Global Biogeochemical Cycles

RESEARCH ARTICLE
10.1029/2018GB006121

Variations in Ocean Deoxygenation Across Earth System Models: Isolating the Role of Parameterized Lateral Mixing

A. Bahl, A. Gnanadesikan[1], and M.-A. Pradal[1]

[1]Department of Earth and Planetary Sciences, Johns Hopkins University, Baltimore, MD, USA

Key Points:
- An intermodel comparison reveals that ocean deoxygenation is sensitive to the representation of lateral mixing
- Stronger lateral mixing results in greater deoxygenation but largely in zones which have high oxygen in the base state
- Intermodel differences of deoxygenation are driven by changes in biological drawdown, which is ultimately controlled by ventilation

Supporting Information:
- Supporting Information S1

Correspondence to:
A. Gnanadesikan,
gnanades@jhu.edu

Citation:
Bahl, A., Gnanadesikan, A., & Pradal, M.-A. (2019). Variations in ocean deoxygenation across Earth system models: Isolating the role of parameterized lateral mixing. *Global Biogeochemical Cycles*, *33*, 703–724. https://doi.org/10.1029/2018GB006121

Received 5 NOV 2018
Accepted 10 MAY 2019
Accepted article online 16 MAY 2019
Published online 13 JUN 2019

Abstract Modern Earth system models (ESMs) disagree on the impacts of anthropogenic global warming on the distribution of oxygen and associated low-oxygen waters. A sensitivity study using the GFDL CM2Mc model points to the representation of lateral mesoscale eddy transport as a potentially important factor in such disagreement. Because mesoscale eddies are smaller than the spatial scale of ESM ocean grids, their impact must be parameterized using a lateral mixing coefficient A_{REDI}. The value of A_{REDI} varies across modern ESMs and nonlinearly impacts oxygen distributions. This study shows that an increase in atmospheric CO_2 results in a decline in productivity and a decrease in ventilation age in the tropics, increasing oxygen concentrations in the upper thermocline. In high latitudes global warming causes shallowing of deep convection, reducing the supply of oxygen to the deep. The net impact of these processes depends on A_{REDI}, with an increase in hypoxic volume yet smaller total deoxygenation in the low-mixing models, but a decrease in hypoxic volume yet larger total deoxygenation in the high-mixing models. All models show decreases in suboxic volume, which are largest in the low-mixing models. A subset of Coupled Model Intercomparison Project Phase 5 models exhibits a similar range of responses to global warming and similar decoupling between total deoxygenation and change in hypoxic volume. Uncertainty in lateral mixing remains an important contributor to uncertainty in projecting ocean deoxygenation.

Plain Language Summary Global warming is expected to change the amount of oxygen present in the oceans, both at the surface and at depth. Some of this is driven by oceanic warming due to an increase in atmospheric temperatures, as warmer water holds less oxygen. But changes in biological drawdown play an even bigger role. Because warmer water is less dense, it becomes more difficult for heavier deep waters rich in nutrients to surface. This reduces biological productivity and in turn means that less organic matter sinks into the deep ocean and rots. Because decomposition uses oxygen, a decrease in decomposition will result in more oxygen at depth. But as oxygen-rich surface waters get lighter, they do not flow as easily into the deep ocean and deliver oxygen to these depths. This causes oxygen to fall. The balance between these three processes determines whether increasing fractions of the deep ocean will become inhospitable to fish and other organisms. The Earth System Models used to project the impacts of climate change predict different balances between these processes. We demonstrate that an important reason for this disagreement is uncertainty in how to represent mixing associated with the oceanic "storms" known as mesoscale eddies.

1. Introduction

Global warming is expected to strongly influence the biogeochemical and physical processes responsible for global oxygen distribution (Cabré et al., 2015; Frölicher et al., 2009; Gnanadesikan et al., 2012; Keeling et al., 2010; Oschlies et al., 2018; Shepherd et al., 2017; Stramma et al., 2010; Vaquer-Sunyer & Duarte, 2008). Three processes are expected to drive changes in oxygen: (i) warming of ocean waters reducing oxygen solubility; (ii) more stratification reducing vertical exchange and the supply of oxygen to the deep, and (iii) weaker vertical exchange reducing the supply of nutrients to the surface, thus driving down both productivity near the surface, and the consumption of oxygen in the ocean interior (Praetorius et al., 2015). Recent work by Schmidtko et al. (2017) demonstrates that the net effect of these three processes (and any additional trends due to decadal variability) has been to reduce global oxygen inventory by 2% since 1960.

Such deoxygenation is of particular concern when it affects the distribution of waters with very low oxygen. In hypoxic waters, many species of heterotrophic zooplankton and air-breathing fish are excluded (Pena et al. 2010; Hsia et al., 2013; Kwon et al., 2016; Schmidtko et al., 2017). The threshold for hypoxia depends

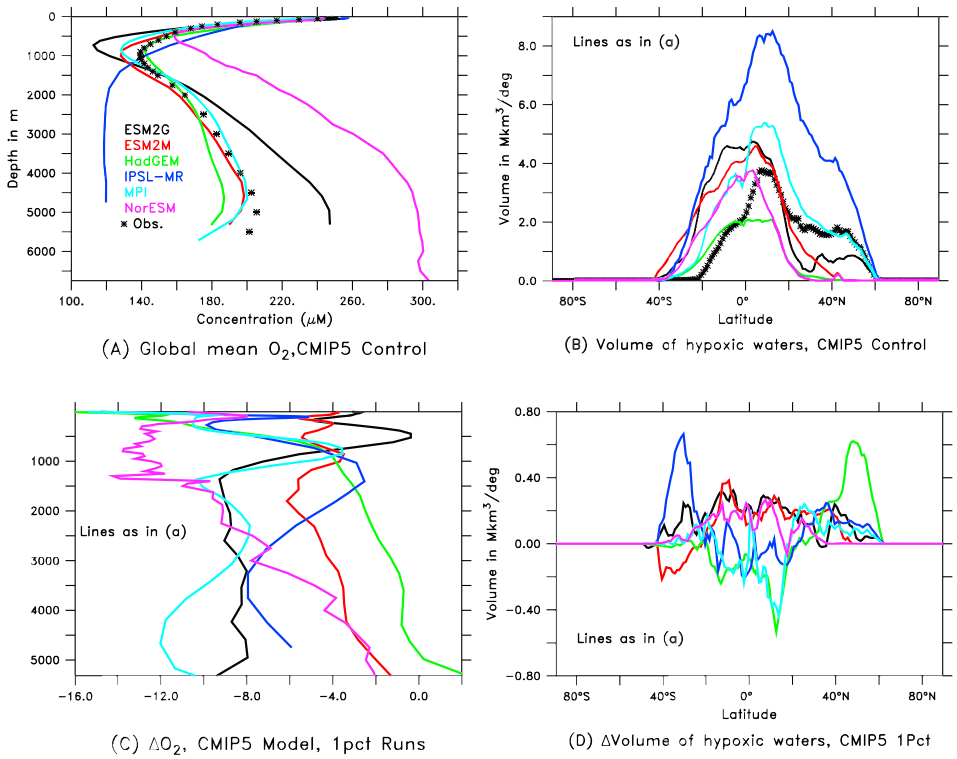

Figure 1. Oxygen in six CMIP5 models: The top panels show the preindustrial control runs compared to observations (symbol) and the bottom panels show changes after a perturbation simulation where atmospheric CO_2 is increased at a rate of 1%/year for 70 years and then held constant for another 70 years (denoted as "1% to doubling"). (a) Horizontally averaged oxygen in control simulations with observations shown by the symbols. (b) Hypoxic volume in Mkm^3/deg in control simulation with observations shown by the symbols. (c) Change in oxygen concentration at end of the 1% to doubling simulations. (d) Change in hypoxic volume at the end of the 1% to doubling simulations. CMIP5 = Coupled Model Intercomparison Project Phase 5.

on the species involved (Mislan et al., 2017; Stramma et al., 2012; Vaquer-Sunyer & Duarte, 2008), but in this study, we choose $O_2 < 88$ μM (~2 ml/L). Hypoxic waters currently make up ~10% of the ocean's total volume. The most extensive regions of hypoxia are found at middepths of the North Pacific, with smaller regions in the North Indian Ocean and the South Pacific Ocean (Bianchi et al., 2012).

Intensely hypoxic (suboxic) waters are strongly associated with denitrification, a microbially facilitated process that converts NO_3^- into gaseous nitrogen, reducing nitrate concentrations while increasing phosphate concentrations. The resulting decrease in the $N^*=NO_3\text{-}16*PO_4$ tracer (Gruber & Sarmiento, 1997) is clearly seen in hydrographic data below oxygen concentrations of 20 μM. We therefore define these waters as suboxic, following previous work by Diaz and Rosenberg (2008) and Gnanadesikan et al. (2013). Approximately ~ 1% of the ocean volume is estimated to be suboxic (Bianchi et al., 2012). Determining future changes in suboxic water volume and the associated changes in denitrification is important because the powerful greenhouse gas N_2O is a byproduct of denitrification (Freing et al., 2012; Nevison et al., 2003). Additionally, denitrification acts to stabilize the ocean nitrogen concentration (Tyrell, 1999).

While many investigators have examined historical trends in ocean oxygen concentration; there is still a need to better understand how to project changes in concentrations into the future. Earth system models (ESMs) are essential tools for making such projections. However, the current generation of models still exhibits large inconsistencies in the simulation of dissolved oxygen (Ying & Yangchun, 2016) and projections of its change under global warming (Bopp et al., 2013).

Such intermodel differences are illustrated in Figure 1, which shows oxygen profiles (left-hand column) and the volume of hypoxic water (Mkm^3/deg latitude, right-hand column) across six models run as part of the Coupled Model Intercomparison Project Phase 5 (CMIP5). A brief description of each model can be found in

Table 1
Summary of CMIP5 Models Shown in Figure 1, Including Biological Model, Value of A_{REDI} Coefficient, and Value of A_{GM} Coefficient

Model	Institute	Ocean biogeochemical model	A_{REDI} (m^2/s)	A_{GM} (m^2/s)
ESM2G	Geophysical Fluid Dynamics Laboratory, NOAA, USA	TOPAZ (Dunne et al., 2013)	BCG closure (50–900)	BCG closure (100–900)
ESM2M	Geophysical Fluid Dynamics Laboratory, NOAA, USA	TOPAZ (Dunne et al., 2013)	600	BCG closure (100–800)
HadGEM2	Met Office Hadley Centre, UK	diat-HadOCC (Palmer & Totterdell, 2001)	500	BCG closure (150–2,000)
IPSL-CM5A-MR	Institute Pierre Simon Laplace, France	PISCES (Wen et al., 2016)	1,000	BCG closure
MPI-ESM-MR	Max Planck Research	HAMOCC5 (Ilyina et al., 2013)	2.5 (10^{-3}) $\cdot\Delta_{x,y}$, Nominal 400	1.6 (10^{-3}) $\cdot\Delta_{x,y}$, Nominal 250
NorESM1-ME	Norwegian Climate Centre, Norway	MICOM (Bentsen et al., 2013)	Equal to near-surface A_{GM}	BCG closure (0–1,500)

Note. BCG denotes closures that scale with the baroclinic growth rate (effectively the vertical shear); in cases where minimum and maximum values are imposed, published values are given in parentheses.

Table 1. A climate change scenario in which atmospheric carbon dioxide is increased by 1%/year for 70 years and then held constant for another 70 years was run for all six cases, with the changes in oxygen and hypoxia shown on the bottom panels of Figure 1. Surprisingly, no simple relationships emerge between the mean state biases and the changes under global warming. Some models (NorESM and MPI), predict significant deoxygenation (Figure 1c) showing a loss of ~10 μM on average, while others lose much less (HadGEM and ESM2M lose ~4 and ~2 μM, respectively). More strikingly, even the sign of the change in hypoxic volume can differ between models (Figure 1d). In particular, the three models with the most realistic profile of oxygen (HadGEM, MPI, and ESM2M) show opposite sign changes in hypoxic volume (with ESM2M increasing hypoxic volume and MPI and HadGEM decreasing it under global warming). Understanding the source of such differences is very difficult, as the ESMs in Figure 1 differ in terms of climate sensitivity, representation of ocean biogeochemistry, and physical dynamics in the ocean.

In this paper, we focus on one process known to vary across models: lateral mesoscale eddy mixing, which, following Redi (1982), is parameterized using a lateral turbulent diffusion coefficient A_{REDI}. Note that while such parametrization is unnecessary in very high-resolution models, such models are generally not run out for long enough times for the solution to reach quasi-equilibrium, rendering their simulations of abyssal oxygen suspect. A_{REDI} varies across ESMs with values ranging from 200 to 4,000 m^2/s (Gnanadesikan et al., 2015b). The differences in A_{REDI} across the CMIP5 models in Figure 1 are shown in the fourth column of Table 1. Little clear relationship can be found with the differences seen in Figure 1. This is consistent with Cabré et al. (2015) who found no correlation between the reported A_{REDI} coefficients and Pacific oxygen minimum zone (OMZ) volumes across CMIP5 models in the mean state. However, by focusing on the impacts of changing A_{REDI} within a single model (in which atmospheric parametrizations and ocean biogeochemistry are identical) we can better isolate which patterns of cross-model variation could be due to uncertainties in this parameter and help explain why changes in oxygen and hypoxic volume appear to be decoupled.

In recent years, our group has examined multiple impacts of changing the A_{REDI} coefficient within a single ESM. This work was motivated by Gnanadesikan et al. (2012) who found that in coarse-resolution ESMs, the mesoscale eddy transport scaled by this parameter is the dominant mechanism supplying oxygen to hypoxic zones. Gnanadesikan et al. (2013) ran a suite of simulations with different spatially constant values of A_{REDI} and found that the value of A_{REDI} was inversely correlated with the volume of hypoxic and suboxic waters. Pradal and Gnanadesikan (2014) found that increasing the mixing coefficient resulted in destabilizing high-latitude haloclines and produced significant surface warming in both the Southern Ocean and North Pacific. Our team extended this work in Gnanadesikan et al. (2015b) to look at the impact of different mixing parameterizations on anthropogenic carbon uptake, also using a new spatially dependent distribution of mixing developed from altimetry measurements.

Until now, we have not analyzed the impact uncertainty in the value of A_{REDI} has on ocean deoxygenation, nor have we looked at the impact of including more realistic spatially varying fields of A_{REDI} on the distribution of oxygen. This paper analyzes and discusses the differences between future projections of ocean oxygen

in the model suite introduced in Gnanadesikan et al. (2015b), with the aim of estimating how much of the difference seen between ESMs could be due to differences in mixing versus differences in biogeochemical formulation or physical climate sensitivity.

The paper is structured as follows. Beginning in section 2, we introduce our model suite including a description of the physical and tracer cycling models used and a mathematical discussion of parameterized subgrid scale turbulent mixing. Section 3 describes the experimental strategy and section 4 discusses the results, starting with an analysis of steady state biases and sensitivities of all the models used in the study. Section 5 examines why the results differ across different models, highlighting both the role of biological utilization of oxygen and the importance of circulation in determining the pattern and magnitude of deoxygenation. Section 6 concludes this paper.

2. Model Description and Physical Background

The ESM used in this study is a lower-resolution version of the National Oceanic and Atmospheric Administration's (NOAA) Geophysical Fluid Dynamics Laboratory (GFDL) ESM2M (Dunne et al., 2012, red lines in Figure 1) denoted as CM2Mc (Galbraith et al., 2011). CM2Mc numerically simulates atmosphere, land surface, sea ice, and ocean dynamics with an exchange grid system that allows for energy, momentum, and tracers to pass between land, sea, ice, and atmosphere every 3 hr. We summarize some of the salient features of this model below. For a more extensive description, the reader is referred to Galbraith et al. (2011).

2.1. Atmosphere Module

The atmosphere module in CM2Mc is based on the GFDL Atmospheric Model, version 2 (AM2, GFDL Global Atmospheric Model Development Team, 2004), and uses a finite volume dynamical core that is virtually identical to that used in the GFDL coupled model CM2.1, but at lower horizontal resolution. The atmosphere grid has a 3.75° longitudinal and a 3° latitudinal resolution with 24 vertical levels and a time step every 1½ hr. The atmospheric physics (aerosols, radiation, and mixing schemes) are in essence identical to ESM2M.

2.2. Ocean Model

The ocean model used is the Modular Ocean Model v4.1 (MOM4p1), code of Griffies et al. (2009), simulating a dynamical core that uses a modified pressure coordinate, allowing for conservation of mass instead of volume, allowing for the use of real freshwater fluxes. The model has a time step every 3 hr and a grid with 28 vertical levels, as well as a 3° longitudinal resolution and a varying latitudinal resolution with an average of about 1.5° and a minimum value of 0.6° in the equatorial latitudes. While this resolution is coarser than each of the CMIP models shown in Figure 1, we will demonstrate that the quality of the simulation is comparable.

Biological cycling is accounted for with the use of a highly parameterized biogeochemical code referred to as BLING: Biogeochemistry with Light, Iron, Nutrients, and Gases (Galbraith et al., 2010). The version of BLING run here includes eight tracers. Six of these are prognostic variables used for evolving the system: dissolved inorganic carbon, alkalinity, micronutrient (nominally Fe), macronutrient (nominally some mix of NO_3 and PO_4), dissolved organic material, and oxygen. These variables are advected and diffused by the same physical processes that advect and diffuse temperature and salinity.

As described in Galbraith et al. (2010), nutrient concentrations and ambient light are used to predict growth rate, from which a parameterized ecosystem (Dunne et al., 2005) is run to compute estimates of biomass and chlorophyll for large and small phytoplankton. These estimates are then used to compute the uptake of nutrients and distribution of light, causing all the biologically active fields to evolve. Oxygen is produced and consumed with a constant stoichiometric ratio of 150:1 relative to phosphorus. The rate of remineralization of sinking biomass is suppressed in low-oxygen waters—an important consideration when analyzing the oxygen budget and its changes under global warming.

Additionally, BLING is run with two "preformed" tracers (DIC_{pre} and $PO4_{pre}$) which are set to the modeled values of DIC and PO_4 in the mixed layer. Below the mixed layer, these tracers are advected and diffused in the same way as DIC and PO_4 but have no source due to remineralization (Ito & Follows, 2005). Thus, the difference between PO_4 and $PO4_{pre}$ gives us the amount of phosphate added (and implicitly oxygen

consumed) by biological activity. We term this tracer $PO4_{remin} = PO_4 - PO4_{pre}$, the remineralized phosphate. Because globally averaged total phosphate is constant, an increase in globally averaged remineralized phosphate must be associated with the mix of waters feeding the deep ocean shifting toward ones with lower preformed phosphate (Marinov et al., 2008). Note that our approach differs from that of Frölicher et al. (2009) who track biologically driven changes in oxygen in terms of phosphate alone—which may shift both as a result of shifting water masses as well as oxygen utilization.

The model is also run with an ideal age tracer. Following Thiele and Sarmiento (1990), the ideal age tracer is set to zero at the first model point in the mixed layer and ages at a rate of 1 year/year thereafter. For instance, if one imagines a pipe running from the well-mixed surface layer to an interior point, the ideal age would be the time required to transit from the surface to that point, sometimes referred to as the ventilation time (England, 1995). In reality, a range of pathways, both advective and diffusive, connect any interior point to the surface and the ideal age is an average of the transit times associated with these pathways.

2.3. Discussion of the Turbulent Diffusion Coefficient, A_{REDI}

CM2Mc, like most ESMs run today, does not resolve spatial scales associated with mesoscale eddies, as they are smaller than the average grid size, and thus requires the lateral transport coefficient to be parameterized. The part of this transport associated with turbulent mixing of tracers along isopycnals (lines of equal potential density) is represented using a Fickian diffusion approximation. The resulting flux of tracer with concentration C, in direction s is given by (Redi, 1982)

$$F_x^C = -A_{\mathrm{REDI}} \frac{\partial C}{\partial s} \tag{1}$$

The resulting flux goes from high to low values of C and is proportional to the size of the tracer gradient. The direction of the flux, ∂s, is taken along isopycnal surfaces within the ocean interior and horizontally in the mixed layer.

In addition to the process parameterized by A_{REDI}, mesoscale eddies produce a net advective flux of tracer along isopycnals. This is accounted for by using a shear-dependent coefficient Gent and McWilliams (A_{GM}) scheme (Gent & McWilliams, 1990; Gent et al., 1995). In regions where isopycnals are strongly tilted, growing eddies flux horizontal momentum downward via form drag. This in turn results in an overturning circulation that flattens isopycnals. The resulting flux of tracer in the x and y direction is

$$F_x^C = -C \times A_{\mathrm{GM}} \frac{\partial S_{x,y}}{\partial z}, \tag{2}$$

where A_{GM} is the diffusive coefficient and $S_{x,y}$ is the slope of the isopycnal in the x and y directions, respectively. The slope is capped at a maximum value of $S_x = 0.01$ to prevent unrealistically large velocities near mixed layers where slopes can become infinite.

As is done in most of the CMIP5 models, A_{GM} is chosen to be proportional to the vertical shear. In our model we use the shear between depths of 100 and 2,000 m to vary A_{GM} between minimum coefficient of 200 m^2/s and maximum coefficient of 1,400 m^2/s so as to produce realistic hydrography and overturning in the Southern Ocean. The resulting global pattern of A_{GM} is shown in Figure 2a. As shown in Table 1, the different CMIP5 models use different minimum and maximum values, though the majority use a broadly similar shear-dependent formulation.

By contrast, there is no consensus across the CMIP5 models on how to specify the A_{REDI} coefficient. A_{REDI} is set equal to A_{GM} in some models (ESM2G, NorESM), to a constant value ranging from 500 (HadGEM) to 1,000 m^2/s (IPSL) in other models, and varies with the grid spacing in the MPI model, with maximum value of 400 m^2/s. While we do not show it here, as it does not have a comparable global warming simulation, the CMCC model of Fogli et al. (2009) uses a constant coefficient of 2,000 m^2/s. While one might expect $A_{\mathrm{REDI}} = A_{\mathrm{GM}}$ as both parametrize mesoscale eddy "mixing," the two coefficients do parameterize different processes (Gent, 2011). Because many models vary A_{REDI} independently of A_{GM} and because we already know it affects OMZs (Gnanadesikan et al., 2013), we focus on this one coefficient at this time.

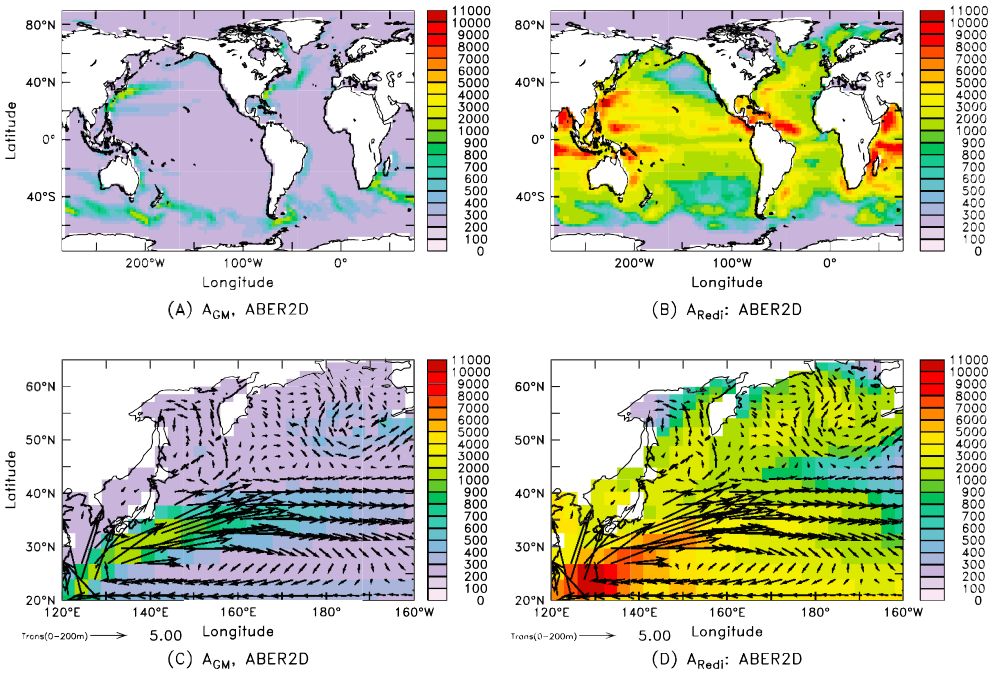

Figure 2. Eddy mixing coefficients in CM2Mc. (a) A_{GM} predicted from the vertical shear between 200 and 1,500 m. (b) A_{REDI} values predicted from altimetry done by Abernathey and Marshall (2013) used in ABER2D simulation. (c) Same as (a) but for NW Pacific (defined as 120°E to 120°W) with transport over top 200 m overlaid. (d) Same as (b) but for NW Pacific with transport over top 200 m overlaid.

3. Experimental Design

A series of six integrations are made to examine the dependence of ocean biogeochemistry on different values of A_{REDI}. Four of the runs use values of A_{REDI} that are constant in space and time: A_{REDI} = 400, 800, 1,200, and 2,400 m^2/s. These runs will often be described as AREDI400 and AREDI800, or low-mixing, and AREDI1200 and AREDI2400, high-mixing. The other two runs use a pattern that varies in space but not in time.

The first of these, denoted as ABER2D, uses a two-dimensional field of A_{REDI} inferred from sea surface height measurements by Abernathey and Marshall (2013). ABER2D's field of A_{REDI} (Figure 2b) is as high as 10,000 m^2/s in high-mixing areas, such as the edges of boundary currents in subtropical gyres, and decreases to very low values in lower mixing regions that are often far from boundary currents, such as the Southern Ocean (Abernathey & Marshall, 2013; see also Gnanadesikan et al., 2015a, Figure 1). It might appear that despite the very different spatial patterns of A_{GM} and A_{REDI} in Figures 2a and 2b, the maximum values of the two are nonetheless colocated. However, a closer look shows that this is not the case. As seen in Figure 2c, which focuses on the Northwest Pacific and overlays surface currents, the baroclinic growth rate parameterization predicts an A_{GM} that is highest in the center of boundary currents and drops to very low values in nearby gyres. However, the Abernathey and Marshall (2013) estimate of A_{REDI} (Figure 2d) shows higher values at the edge of the currents and lower values in the center (see Klocker & Abernathey, 2014, for an explanation of why this occurs).

Finally, the last experiment uses a zonally averaged version of the ABER2D parameterization, denoted as ABERZONAL. This is used to determine whether the full two-dimensional structure of the A_{REDI} field is most important or simply the variation with latitude (which might be more constant in time and thus more easily applied to simulate past climates). Although these spatially varying fields of A_{REDI} have been used in previous work in our group (Gnanadesikan et al., 2015a, 2015b; Gnanadesikan, Russell, et al., 2017), they are substantially different than the distributions of A_{REDI} used in all the CMIP5 models and their impact on oxygen fields has not been previously documented.

Our control run (AREDI800) was initialized with temperature, salinity, phosphate, oxygen, and DIC from modern hydrographic data and spun up for 1,500 years with orbital parameters, solar flux, atmospheric greenhouse gasses, and aerosols held at "preindustrial" year 1860. Once the simulations reached year 1500, the additional five scenarios (AREDI400, AREDI1200, AREDI2400, ABER2D, and ABERZONAL) were branched off the control. All six simulations were then continued for 500 years with constant solar fluxes, aerosols, and greenhouse gases. At model year 1860 (360 years into the new control) additional runs are made in which the concentration of CO_2 is instantaneously doubled from the preindustrial value of 286 ppmv to a value of 572 ppmv for both CO_2 and radiation schemes. These simulations were run out for an additional 140 years. Instantaneously doubling atmospheric CO_2 allows us to estimate the forced component of climate change and how this component is reflected in ocean circulation. Instantaneously doubling CO_2 in an ESM is an idealization that removes variation on the time scales associated with CO_2 growth. However, it also introduces a "shock" to the system that might not be reflected in historical simulations.

4. Results

4.1. Steady State Differences

We begin by repeating the steady state analyses shown in Figure 1 for our model suite. As was the case for the CMIP5 models, horizontally averaged oxygen (Figure 3a) is very similar at the surface, with differences starting to appear at 500 m. All six models simulate the general shape and mean value throughout the water column with better skill than the IPSL and NorESM models (Figure 1a). Among our models, ABERZONAL and AREDI1200 best capture the shape of observational data, shown in Figure 3a, and simulate mean oxygen concentrations (Table 2, column 3) that are relatively close to the global average observational value of 177.1 μM.

Although some of the cross-model differences in oxygen are attributable to temperature, the fraction is relatively small. Higher mixing in our suite is associated with more realistic lower global mean temperatures (Table 2, column 2). The 0.6°C decrease in temperature between AREDI400 and ARED2400 (Table 2, column 2) is only enough to produce a 1.4% change in solubility. Assuming sinking waters are in perfect equilibrium, this would produce a 4-μM increase in oxygen concentration (a small fraction of the 31 μM we are trying to explain).). Conversely, the difference in remineralized phosphate between AREDI400 and AREDI2400 (Table 2, column 5) is 0.24 μM. Given the O_2:P stoichiometric ratio of 150:1, the expected increase in oxygen would be 36 μM. The sum of these two distinct elemental processes predicts a change in oxygen larger than what is seen across the models because we have neglected gas exchange. The waters sinking into the deep ocean are not, in fact, fully equilibrated with the atmosphere (as also noted by Frölicher et al., 2009).

These globally integrated measures of oxygen bias smooth over significant spatial variability. At 300 m (Figure 4), all of the models show similar patterns of errors, with an overestimate of oxygen concentrations around the edges of the North Pacific subtropical gyre and the Arabian Sea and underestimates of oxygen in the Benguela upwelling, Gulf of Guinea and between 40 and 60°S in the Indian sector of the Southern Ocean. Differences are found across the models in the South China Sea (where oxygen is strongly underestimated in the low-mixing cases). Subtler differences are found in the OMZs in the Pacific and around Antarctica, where the concentrations increase by 20–40 μM as the mixing increases. The patterns of bias in the subpolar North Pacific are seen in four of the six CMIP5 models (Figure S1), but the patterns of bias in the Atlantic and Southern Oceans are much less consistent in the CMIP5 suite, with some models greatly overestimating oxygen in these regions and others underestimating it.

At 3,000 m by contrast (Figure 5) the pattern of error is quite different across the different models in our suite, with higher mixing being associated with large overestimates of oxygen in the deep Northwest Pacific. The cause of this overestimate, previously discussed in Gnanadesikan et al. (2015a) is the presence of excessively deep overturning in that region, a point to which we will return later. More subtly, most of the models in the suite underestimate oxygen below the OMZs in the tropical Pacific, with the lowest mixing models showing the greatest bias. The latter bias is also seen in all of the CMIP5 models (Figure S2).

Hypoxic and suboxic volumes vary significantly across the CM2Mc model suite, (Table 2, columns 3 and 4). As previously noted in Gnanadesikan et al. (2013) low-mixing models, especially AREDI400, greatly

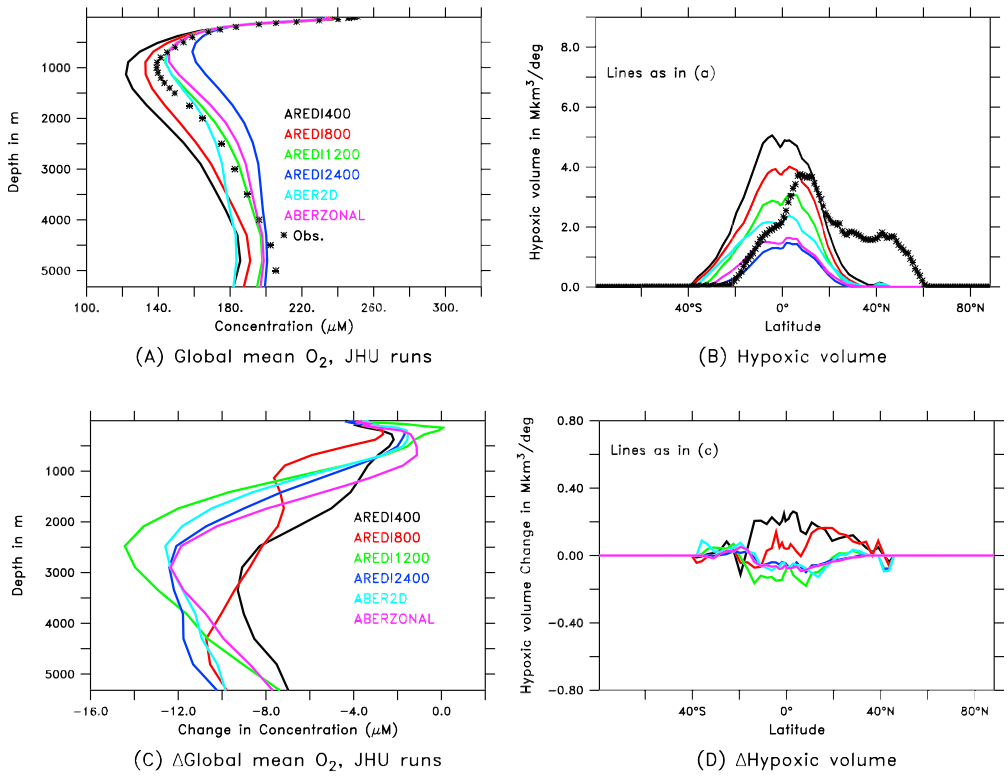

Figure 3. Same as Figure 1 but for CM2Mc model suite. JHU = Johns Hopkins University.

overestimate hypoxic and suboxic volume compared to observations, while high-mixing models, specifically AREDI2400, greatly underestimate them. Despite having very large peak diffusivities, the ABER2D and ABERZONAL models tend to have less oxygen and more hypoxia than the AREDI2400 case. Note that there is a big difference in suboxic volume between ABERZONAL and ABER2D, implying that the full two-dimensional structure of the mixing coefficient matters for capturing these biogeochemically important waters. As shown in Figure S3 the hypoxic waters in our model suite are centered in the tropics —with none of the models capturing observed hypoxia in the North Pacific. The models all fail to capture the separation between the northern and southern OMZs.

Our model suite produces three-dimensional temperature, salinity, and oxygen fields, which are comparable in accuracy to those from the CMIP5 models. As shown in the Taylor diagrams in Figure 6, our simulations of oxygen lie between the worst-correlated model (NorESM, with a value of 0.65) and the best (MPI, with a value of 0.92). AREDI1200, ABER2D, ABERZONAL, and AREDI2400 produce nearly identical correlations

Table 2
Globally Averaged Temperature, Globally Averaged O_2 Concentration, Globally Integrated Volume of Hypoxic Waters ($O_2 < 88\ \mu M$) and Suboxic Waters ($O_2 < 20\ \mu M$), and Globally Averaged Remineralized Phosphate Concentration for Six Parameterizations of A_{REDI} Run in CM2Mc

A_{REDI} (m^2/s)	Global average temperature (°C)	O_2 concentration (μM/kg)	Volume of $O_2 < 88$ μM (Mkm^3)	Volume of $O_2 < 20$ μM (Mkm^3)	Remineralized phosphate ($PO4\text{-}PO4_{pre}$, μM)
Obs.	3.660	177.1	150.1	17.70	N/A
400	4.846	154.7	182. 6	51.28	0.905
800	4.604	161.4	141.8	31.39	0.844
1,200	4.379	173.5	102.1	20.10	0.755
2,400	4.244	185.5	42.71	5.450	0.661
2D	4.604	168.3	87.0	13.3	0.775
Zonal	4.448	176.7	53.9	4.84	0.750

Note. Model results are from a 100-year average of the control simulation. There are no observations of preformed phosphate available.

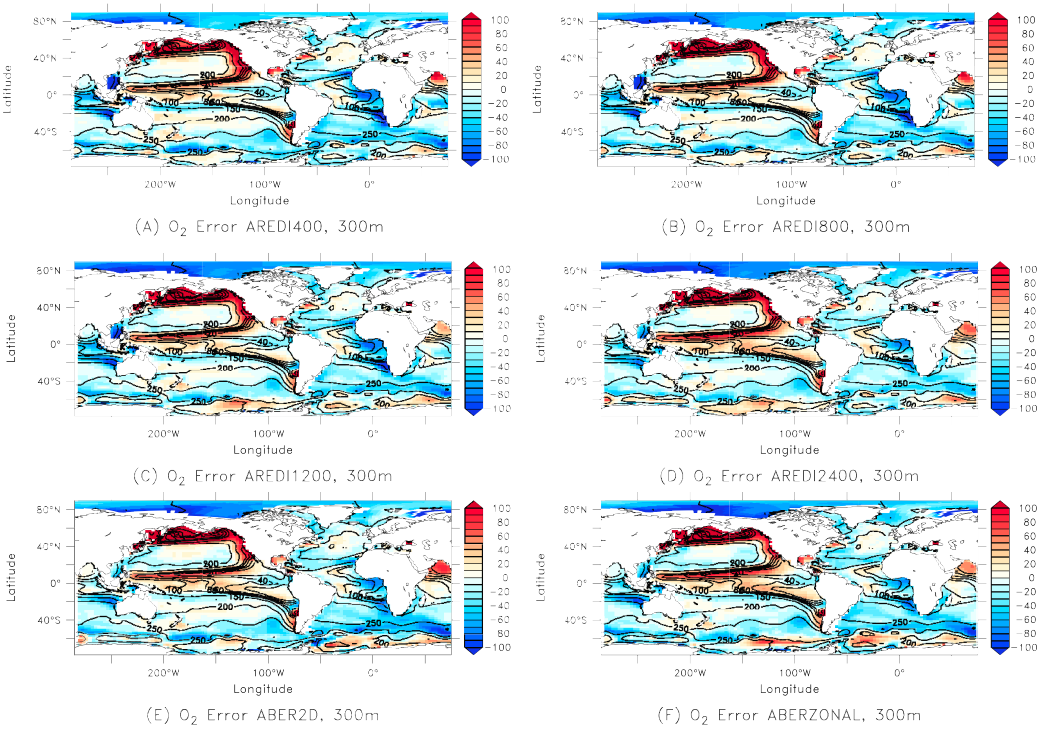

Figure 4. Bias in oxygen concentrations at 300m (μM, colors) in preindustrial control simulations from CM2Mc models with different mixing coefficients. Contours show the climatological concentration of oxygen with contours every 20 to 100 μM and 50 μM above that. (a) AREDI400, (b) AREDI800, (c) AREDI1200, (d) ARED2400, (e) ABER2D, (f) ABERZONAL.

of 0.7. The CMIP5 models generally overestimate the global range (with the exception of HadGEM2) while our models underestimate it. In terms of RMS error (distance from the 1,0 point) the AREDI400 simulation is comparable to the best of the CMIP5 simulations examined here.

In both our model suite and in the CMIP5 models the models that produce the best salinity fields (AREDI2400 and IPSL-MR, respectively) are not the ones with the best spatial distribution of oxygen. Similarly, the models with the best simulation of oxygen distribution do not necessarily capture hypoxic and suboxic volume. The AREDI1200 model has less mean bias than AREDI400 in oxygen and hypoxic volume (Table 2), but a pattern of variation that is less correlated with observations. Similarly, MPI has a pattern of oxygen that is well-correlated but an amplitude of variation that is too large. This overestimate of the magnitude of variability is reflected in an overestimate of the hypoxic volume. As a result, which model produces the "best" simulation (both for the CMIP5 models and our suite) depends on which metric is used.

4.2. Deoxygenation Under Doubled Atmospheric CO_2

The ocean's response to doubled CO_2 also depends on the choice of A_{REDI}. The data in Table 3 list the changes in temperature, oxygen, hypoxic and suboxic volumes, and remineralized phosphate across the models after 140 years of doubled CO_2. In contrast to the control, where models simulate a clear inverse relationship between O_2 concentration and hypoxic volume, a larger decrease in mean oxygen concentration is not predictive of a larger decrease in hypoxic volume. As can be seen from Figures 3c and 3d, large absolute differences between models are seen at depths of ~300 m and at ~3,000 m (which will motivate further analysis in section 5). Columns 3 and 4 in Table 3 show that the largest change in total O_2 concentration is seen in AREDI1200 (−9.4 μM) and the smallest in AREDI400 (−6.2 μM), a smaller range than in the CMIP5 models. Based on the inverse relationship described in the steady state, we would therefore expect AREDI1200 to show the largest increase in hypoxic volume. Instead, low-mixing models increase the volume of hypoxic waters, while high-mixing and spatially dependent models decrease the volume (Table 3, column 3 and Figure 3d). The range of zonally integrated changes in hypoxic volume seen in CMIP5 models (Figure 1d)

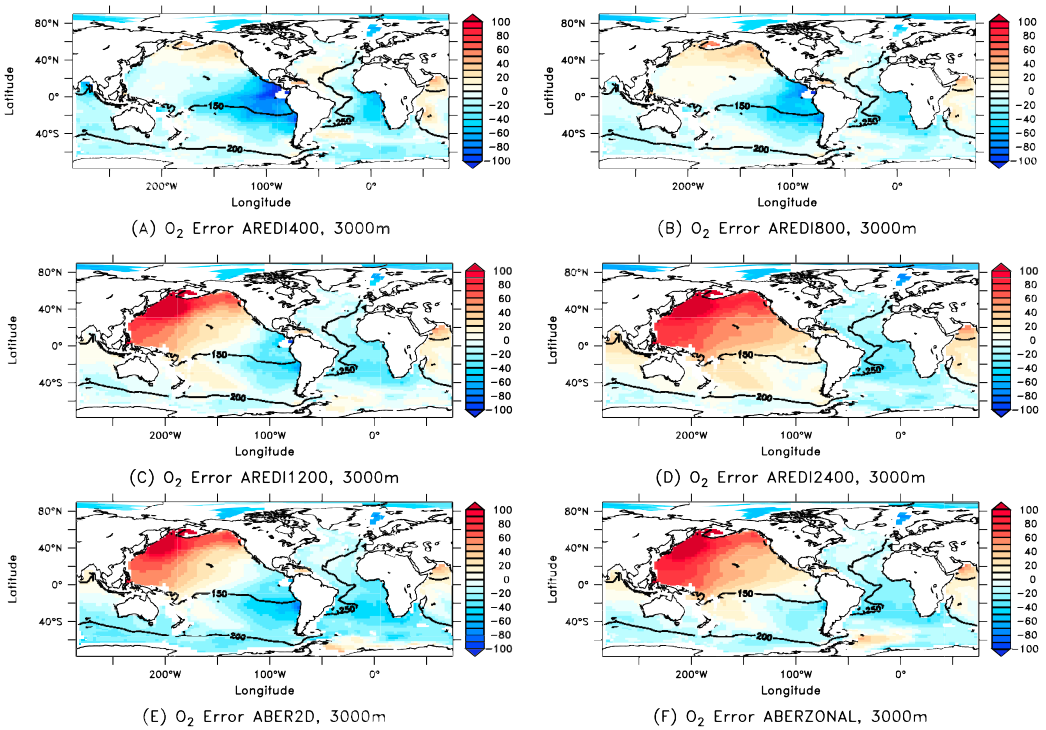

Figure 5. Bias in oxygen concentrations at 3000m (μM, colors) in preindustrial control simulations from CM2Mc models with different mixing coefficients. Contours show the climatological concentration of oxygen with contours every 50 μM. (a) AREDI400, (b) AREDI800, (c) AREDI1200, (d) ARED2400, (e) ABER2D, (f) ABERZONAL.

is larger than the CM2Mc model spread in Figure 3d and shows changes in extratropical latitudes that are not seen in our suite. There is a similar range of changes in the tropics. Clearly, understanding what drives cross-model differences in oxygen distribution in the preindustrial control, deoxygenation under global warming and the relationship between the two requires further analysis.

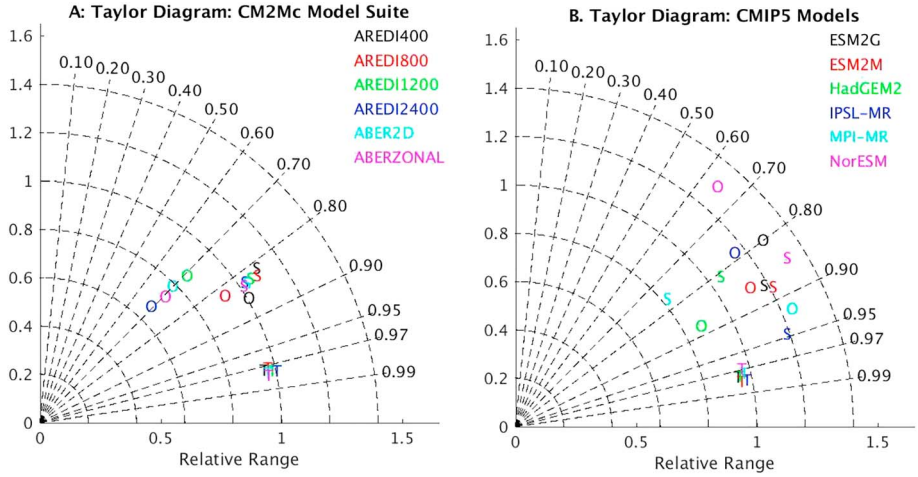

Figure 6. Taylor diagram evaluating fit to observations for temperature (*T*), salinity (*S*), and oxygen (O) concentrations relative to World Ocean Atlas 2009. (a) In CM2Mc models for a century average from the 400th–500th year of the model spin-up. (b) For the CMIP5 models in Figure 1. The radial coordinate shows the normalized standard deviation, angle shows correlation. A model perfectly matching observations would lie at coordinate [1,0]. The further from this point, the higher the root-mean-square error. CMIP5 = Coupled Model Intercomparison Project Phase 5.

Table 3
Global Average Changes in Temperature, Oxygen, and Remineralized Phosphate and Globally Integrated Changes in Hypoxic and Suboxic Volume 140 Years After Instantaneous CO_2 Doubling

A_{REDI} (m^2/s)	Temperature change (°C)	O_2 concentration change (μM)	Volume of O_2 < 88 μM change (Mkm^3)	Volume of O_2 < 20 μM change (Mkm^3)	Remineralized Phosphate ($PO4\text{-}PO4_{pre}$) change (μM)
400	0.43	−6.2	8.3	−1.8	0.033
800	0.42	−7.7	3.3	−2.3	0.046
1,200	0.42	−9.4	−4.0	−2.7	0.056
2,400	0.39	−8.6	−2.4	−1.1	0.050
2D	0.42	−8.8	−1.5	−1.8	0.051
Zonal	0.41	−7.6	−2.0	−1.1	0.041

5. Discussion

We approach this analysis in four parts. First, we demonstrate that intermodel differences in deoxygenation are driven by differences in how biological drawdown changes, not to differences in solubility. Second, we demonstrate that the pattern of change in deoxygenation can be readily related to changes in the rate of ventilation. Third, we show that such differences in ventilation across models are driven by differences in overturning, primarily in the North Pacific. We then discuss how the three-dimensional structure of changes in oxygen, relative to the location of hypoxic and suboxic waters, produces contrasting results for the high- and low-mixing cases. Finally, we show that an important way in which mixing affects oxygen is through changing the salinity stratification and lateral salt transport in high latitudes.

5.1. Understanding Cross-Model Differences in Deoxygenation

5.1.1. Temperature and Solubility

The globally averaged temperature across the six models under global warming (Table 3, column 1) changes by almost the same amount across all models. The limited model spread comes as a major surprise given that the differing extents of sea ice in the preindustrial state (Pradal & Gnanadesikan, 2014) would be expected to produce different magnitudes of ice-albedo feedback. However, full analysis of this result is beyond the scope of this paper. For now, we note that the globally integrated warming of 0.4 °C across the suite neither explains the size of the changes in oxygen nor its dependence on A_{REDI}. Such warming would be expected to produce a 3.2-μM change in oxygen saturation, which only accounts for one fourth to one half of the changes seen in the models.

This finding is consistent with Bopp et al. (2002) and Matear and Hirst (2003), who found that only approximately one fourth of the oxygen depletion in their global warming simulations could be attributed to solubility changes. Likewise, Schmidtko et al. (2017) attributes less than half of deep oxygen changes to temperature, although they did find strong solubility-induced changes in the surface layers. But these studies differ from Frölicher et al. (2009) who found the majority of deoxygenation to be associated with changing solubility. Similarly, we recognize that thermally driven differences in deoxygenation could still be important on regional scales.

5.1.2. Changes in Biological Oxygen Utilization

As was true for our control simulations, intermodel differences in deoxygenation under global warming are largely due to differences in biological oxygen utilization. AREDI400 simulates a 0.033-μM increase in remineralized phosphate while AREDI2400 simulates a 0.056-μM increase. Given a 150:1 ratio of oxygen to phosphate, the 0.023-μM difference in the increase would be expected to produce a difference of 3.6-μM O_2 between the two models, similar in magnitude to the 3.2-μM difference actually seen. If both the changes in temperature and remineralized phosphate were fully expressed in the AREDI1200 case (which sees the biggest change), we would expect to see a 11.6-μM decrease in oxygen concentration. However, in the presence of finite gas exchange the actual change of 9.4 μM (Table 3, column 2) is only 80% of the potential decrease.

Although changes in oxygen utilization explain the greater portion of the differences across both the control and global warming simulations, there are two possible reasons for such differences. The biological drawdown of oxygen can be thought of as ~150 times the inventory of remineralized phosphate. This in turn can be written as the flux of organic phosphorus to the deep ocean multiplied by its residence time.

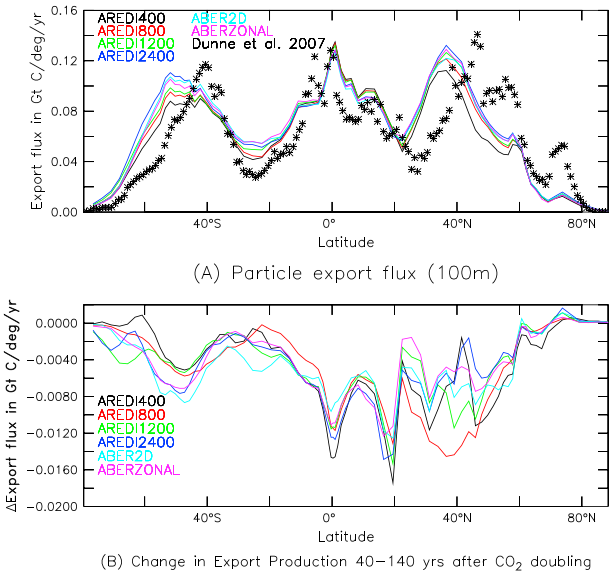

Figure 7. Zonally integrated particle export flux at 100 m across the CM2Mc model suite in Gt C/deg/year) compared to observations (symbols) from Dunne et al. (2007). (a) Control model. (b) Change over years 40–140 after instantaneous doubling of CO_2.

Changes and differences in the drawdown of oxygen can thus be driven by changes and difference in the flux of organic phosphorus to the deep, or in the age of deep waters. In the following section we explore which of these drivers is most important.

5.2. Understanding Differences in Biological Utilization

5.2.1. Export Production

Cross-model differences in export production across models are relatively small under both our control (Figure 7a and Table 4) and global warming (Figure 7b and Table 4) scenarios, showing that they cannot account for cross-model differences in oxygen inventory. Globally integrated export fluxes vary from 9.95 GtC/year in AREDI400 to 11.1 GtC/year in AREDI2400, well within the 9.8 +/2 GtC/year estimated by Dunne et al. (2007, symbols in Figure 6a). The regional pattern of export differs across the model suite, with noticeable latitudinal shifts relative to observations. Oxygen concentrations are 20% higher in AREDI2400 than in AREDI400 (Table 3, column 3), even though the export flux (and thus deep oxygen consumption) is 10% higher in AREDI2400 (Table 4). The higher deep ocean oxygen in AREDI2400 must therefore be driven by greater physical exchange between the surface and deep ocean, resulting in a larger oxygen supply to the deep.

Doubling CO_2 results in a decrease in export across all model runs, with the global decline being fairly similar across all models (7–10%). Zonally averaged changes vary most in Northern midlatitudes (around 40°N), with the largest decline being seen in AREDI800. On a basin scale, the largest range of changes is seen in the North Pacific, where AREDI1200 produces a decline of −0.20 Gt C/year while ABERZONAL produces a decline of −0.05 Gt C/year. While the consistent decline in export production across all latitudes would be expected to cause a decrease in remineralized phosphate, the opposite (with a concomitant decrease in oxygen) is actually seen.

5.2.2. Ventilation

Export production cannot explain even the sign of the differences in oxygen concentration across models. Nor can it explain the sign of (or different magnitudes of) the changes in oxygen concentration under global warming. We therefore turn to differences in ventilation as diagnosed by differences in age.

In Figure 8, we compare changes of O_2 and ideal age under doubled CO_2 in each of the models at 300 m—one of the depths where large cross-model differences are seen in Figure 3c. Oxygen decreases as age increases across each of the models, with AREDI800 simulating the strongest correlation of −0.84. All the models show oxygen increasing and age decreasing in the tropics. Away from the tropics, we see clear differences between the models in the western Pacific and the Southern Ocean. Although the size of the effect varies across models, all the models exhibit increases in age and decreases in oxygen in these regions. In the Northwest Pacific, the largest changes are found in AREDI400 and AREDI800, while in the Southern Ocean, the biggest changes are found in the ABERZONAL model.

Table 4
Export Production in Model Suite and Observation in Gt C/year

	Global	Atlantic 30–65°N	Pacific 30–65°N	Southern Ocean <30°S	Tropics 30°S to 30°N
Satellite	9.8 ± 20%	1.1	1.5	2.4	3.9
AREDI400	9.95 (−0.73)	1.31 (−0.14)	1.14 (−0.12)	2.69 (−0.09)	5.01 (−0.45)
AREDI800	10.4 (−0.78)	1.31 (−0.09)	1.43 (−0.22)	2.86 (−0.14)	5.02 (−0.39)
AEDI1200	10.7 (−0.73)	1.26 (−0.04)	1.56 (−0.20)	2.96 (−0.15)	5.12 (−0.39)
AREDI2400	11.1 (−0.73)	1.28 (−0.08)	1.65 (−0.09)	3.25 (−0.17)	5.08 (−0.44)
ABER2D	10.9 (−0.78)	1.25 (−0.06)	1.62 (−0.18)	3.14 (−0.20)	5.13 (−0.41)
ABERZONAL	10.9 (−0.67)	1.26 (−0.13)	1.60 (−0.05)	3.04 (−0.16)	5.21 (−0.37)

Note. Model results are shown using 100-year average climatology and across a depth of 100 m. Changes for years 40–140 after doubling are shown in parentheses.

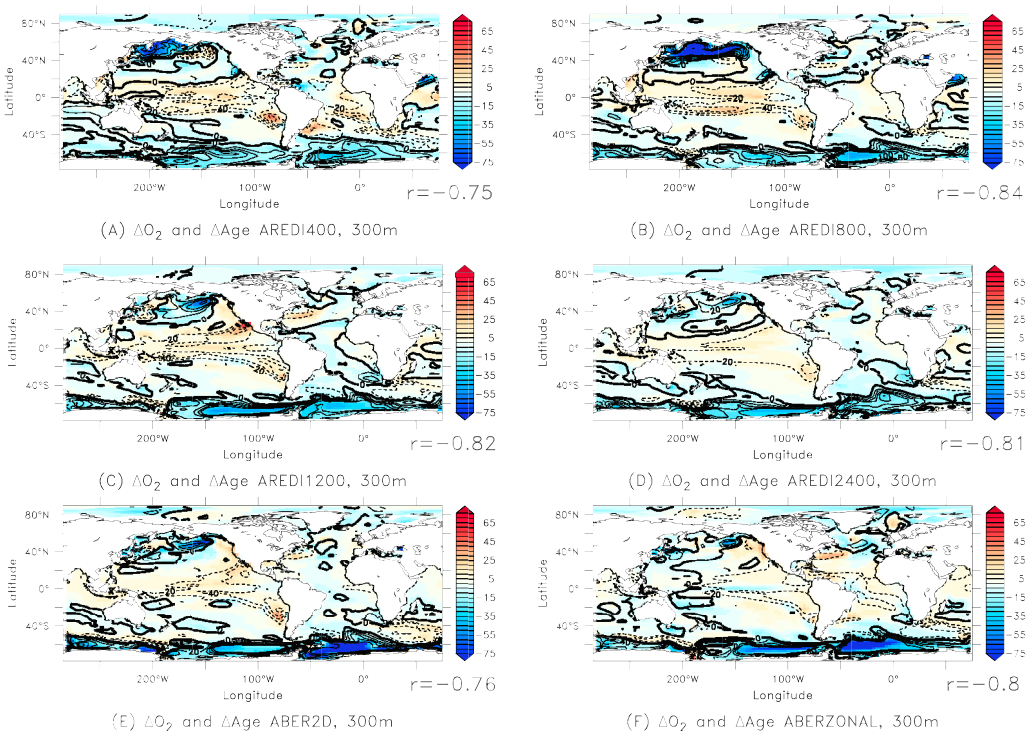

Figure 8. Changes in the distribution of oxygen concentration (colors, μM) and age (contours, year) at 300 m 140 years after doubling CO_2 across our suite of simulations. Contour range is from −100 to 100 years by 20 years. The low-mixing cases (AREDI400 and AREDI800, panels a and b) show the largest depletion in the North Pacific at this depth. The two spatially varying cases, (ABER2D and ABERZONAL, panels e and f) simulate large changes in the Southern Ocean. Changes in the higher mixing models (AREDI1200 and AREDI2400, panels c and d) are generally smaller in high latitudes and larger in low latitudes.

At a depth of 3,000 m (Figure 9), a similarly high correlation between changes in ideal age and oxygen is exhibited across the model suite. The high-mixing models exhibit the strongest correlation with AREDI1200 at −0.98 and AREDI2400 at −0.97. Significant differences across the models are seen in the Northwest Pacific with the high-mixing models (AREDI1200, AREDI2400, ABER2D, and ABERZONAL), all showing declines in oxygen concentration of more than 75 μM and increases in age by hundreds of years. The large changes in age in both the Southern Ocean and North Pacific point to a strong decline in vertical exchange. Note that the North Pacific changes amount to a reversal of biases seen in Figure 5.

An important part of the vertical exchange across our model suite is the deep overturning circulation. As shown by the contour plots in Figure 10, the high-mixing models all produce a strong overturning circulation in the North Pacific, which penetrates over a substantial fraction of the water column. As described in previous work (Gnanadesikan et al., 2015a, 2015b, 2017), this circulation bias produces waters at depths that are too young, excessively depleted in radiocarbon, and have overly high concentrations of anthropogenic carbon. Under global warming (colors in Figure 10), this circulation slows and shallows substantially. As a result, waters at depth in the North Pacific are now associated with much older Antarctic Bottom Waters, resulting in an increase in age and decrease in oxygen. In the low-mixing models, however, the Antarctic Bottom Water cell in the Indian and Pacific becomes more compressed below 1,000 m but does not weaken substantially. As a result, deep oxygen and age in the low-mixing models are relatively unchanged under global warming.

At 300 m, the picture is more complicated. In low-mixing models (AREDI400 and AREDI800), the North Pacific overturning collapses under global warming and thus increases in age and decreases in oxygen are found in these simulations. In AREDI2400 and ABERZONAL, although the maximum overturning weakens by ~50%, the resulting overturning is still relatively strong compared with observation. As a result, the changes in age and oxygen in these two models at 300 m are relatively weak (Figures 8d and 8f). The

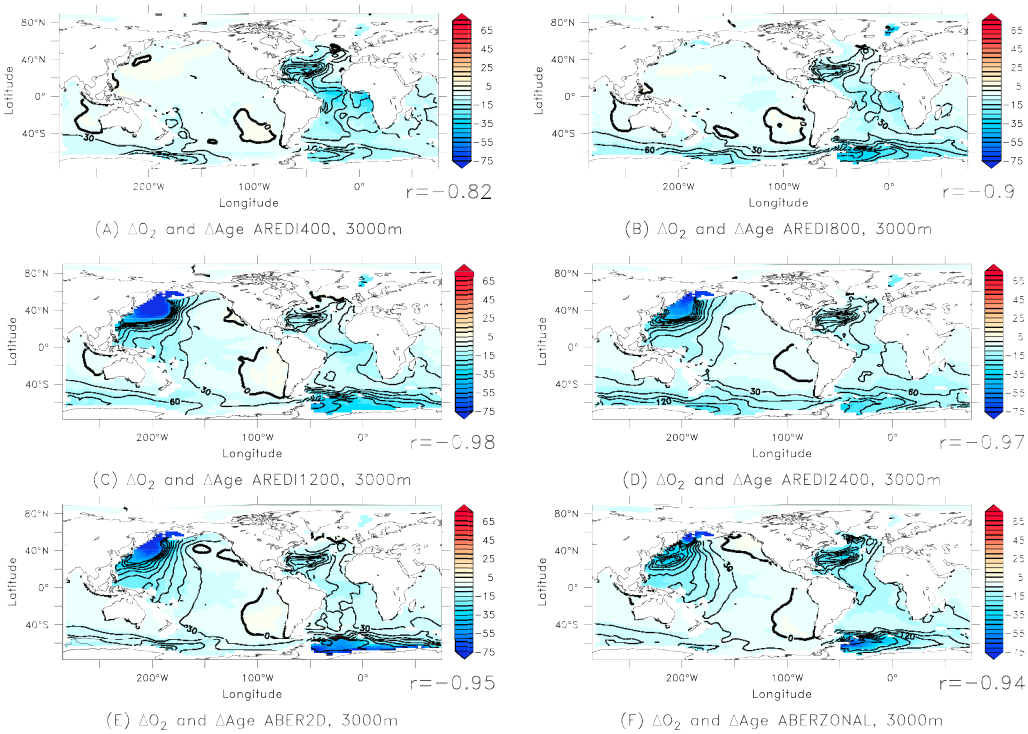

Figure 9. Changes in oxygen concentration (μM) and age at 3,000 m 140 years after doubling CO_2 across suite of simulations. Contour range is increased at this depth from −300 to 300 years by 30. The high-mixing models (c, d) experience a significant decline in oxygen concentration in the Northwest Pacific, corresponding to the regions where they also show a positive bias in their control simulations (Figure 5), while the low-mixing cases (a, b) experience no change/increases at 3,000-m depth in this region. The spatially variable mixing runs (e, f) produce similar results to high-mixing models.

biggest changes in overturning in these two cases are found below the depth of the maximum overturning and thus represent a shallowing overturning. The AREDI1200 and ABER2D models lie in between these two extremes, with a strong overturning that largely collapses under global warming.

In the tropical Pacific, all of the models show an increase in oxygen concentration and a decrease in age. This phenomenon of simultaneous decreases in overturning and age has previously been discussed in Gnanadesikan et al. (2007). It is due to the fact that waters at this depth receive inputs both from a "slow pathway" due to an upwelling of old waters from below, as well as from a "fast pathway" in which young waters located at the surface are mixed downward. Mean age is determined by both the characteristic timescales of the two pathways and the fractional contribution from each of them to ventilation at a point. A change in circulation which decreases the "fast pathway" by a little, but the "slow pathway" by a lot will make an interior parcel more like the surface and will produce a decrease of age even as the circulation decreases. As shown in Gnanadesikan et al. (2012), similar changes in the pathways by which oxygen is supplied to intermediate depths (less oxygen-depleted water coming up from below relative to oxygen being mixed down from above) help to explain increases in oxygen in suboxic waters under global warming.

While all the models show a decline in tropical upwelling, the waters contributing to this decline differ across the model suite. In the low-mixing models the decline in upwelling is associated with Antarctic Bottom Water and the decrease in age exceeds 40 years in many locations. In the high-mixing models the decline in overturning is more associated with slowing of the North Pacific Cell and the increase in age and decrease in oxygen are smaller.

The Southern Ocean shows similar linkages between changes in age and oxygen, with increases in age and decreases in oxygen in both the Weddell and Ross Seas. At 300 m, the largest changes in oxygen and age in the Ross Sea are seen in the AREDI1200 case, whereas in the Weddell the largest changes are found in ABER2D and ABERZONAL which have relatively small mixing coefficients in the Southern Ocean (Figure 2b). At 3,000 m, the biggest changes are seen in the Weddell Sea.

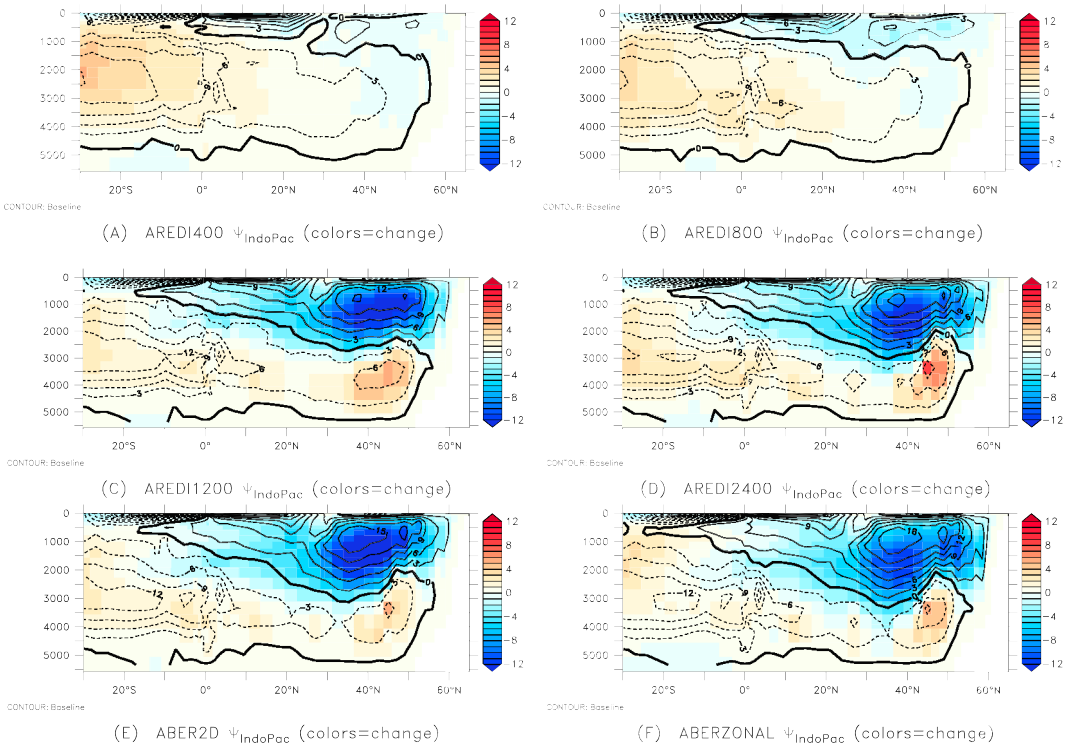

Figure 10. Meridional overturning circulation in Sv (contours) and its change under global warming (colors) for the Indian and Pacific Oceans. (a) AREDI400, (b) AREDI800, (c) AREDI1200, (d) AREDI2400, (e) ABER2D, (f) ABERZONAL.

The mechanisms behind the changes in the Southern Ocean are hard to isolate. The overturning in this region varies much less with mixing coefficient across the preindustrial control models in the Southern Ocean (Figure S4) than it does in the North Pacific (Figure 10). Under global warming all models show a decrease in the lower overturning cell associated with Antarctic Bottom Water but an increase in the upper cell associated with the transformation of Circumpolar Deep Water to light surface waters. While we will return to the Southern Ocean in sections 5.4 and 5.5, a full analysis of the changes must wait for a future manuscript focusing on the sensitivity of Southern Ocean convection to eddy parameterization.

5.3. Understanding Why Changes in Oxygen and Hypoxic/Suboxic Volume Are Decoupled

The complex, three-dimensional structure of changes in oxygen concentrations helps to explain why the total amount of deoxygenation (largest in the high-mixing models) does not match the changes in hypoxic and suboxic volume (biggest increases found in the low-mixing models). If we take the zonal integral of oxygen change (contours Figure 11), we see tongues of lower oxygen penetrating into the deep ocean from high latitudes, associated with the changes in ventilation seen in Figures 8–10. The biggest changes are seen in the AREDI1200 model, in which an initially strong overturning in the North Pacific shuts off under global warming. By contrast AREDI400 has relatively little overturning in the North Pacific and so exhibits little change, while AREDI2400 shows a shallowing but not a complete shutoff of overturning and so shows less change at shallow depths. We also see an increase in oxygen in the middepth tropics associated with less upwelling of old waters from below.

These changes map onto the baseline oxygen fields in different ways in the different models. By setting a tracer of hypoxia to a value of 1 and integrating zonally, we are able to get a measure of the length subtended by hypoxic waters and to look at how this length changes under global warming (colors, Figure 11). In the AREDI400 simulation, the waters at depth, particularly in the Eastern Pacific, are close to being hypoxic due to being biased low in the control simulation (Figure 5). The changes in deep oxygen associated with a slower overturning push these waters over the edge into hypoxia. As the mixing increases, the deep oxygen in the control simulations is further away from hypoxia (Figures 5c–5f). Thus, even though the decline in

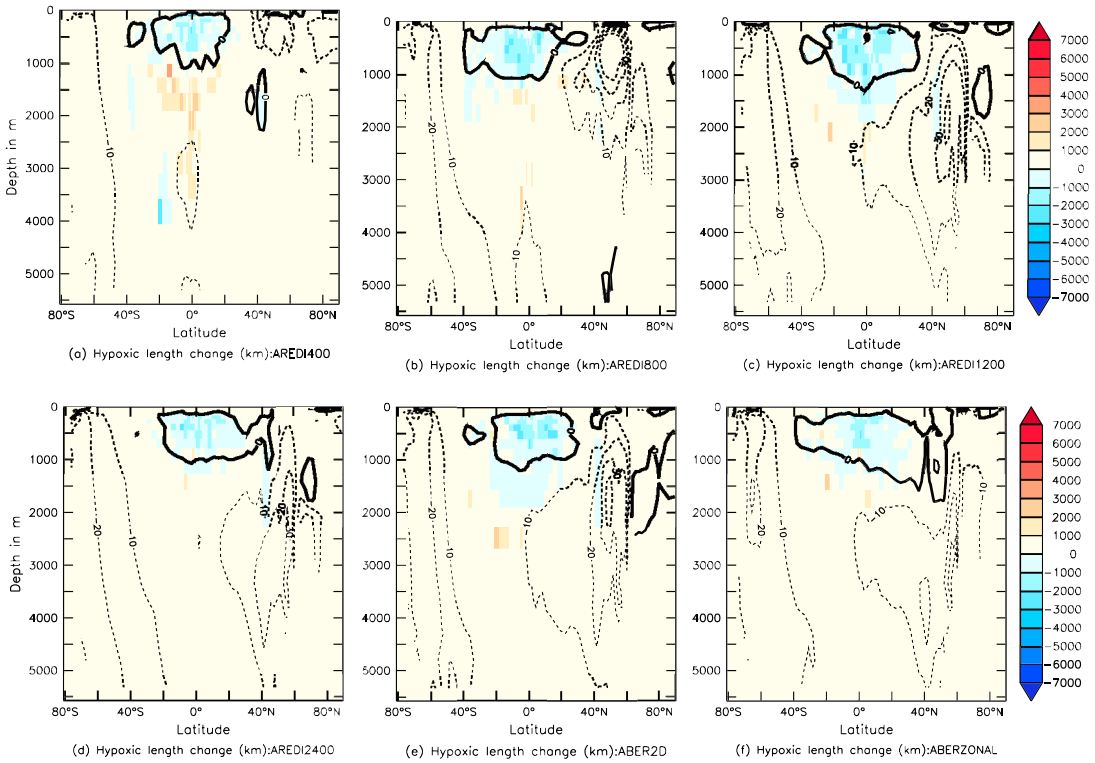

Figure 11. Zonally integrated changes in oxygen and hypoxic volume after 140 years of doubled CO_2 in CM2Mc model suite. Contours show change in oxygen concentration in μM. Colors are found by setting a tracer to 1 when waters are hypoxic and integrating zonally, producing a length subtended by hypoxic waters. (a) AREDI400, (b) AREDI800, (c) AREDI1200, (d) AREDI2400, (e) ABER2D, (f) ABERZONAL.

oxygen concentration in these simulations is larger, we do not see an increase in hypoxia in the abyss. Instead, these simulations are dominated by the decrease in hypoxia associated with the increase in middepth oxygen. The suboxic volumes similarly decrease across all six simulations since (outside of the Black Sea) our model only has suboxic waters in the upper water column where oxygen increases under global warming.

5.4. Explaining Sensitivity of Vertical Exchange to Lateral Mixing

5.4.1. Stratification

While we have demonstrated that A_{REDI} affects oxygen largely through modulating vertical exchange, we have not explained how this modulation occurs. As noted in Pradal and Gnanadesikan (2014), differences in vertical exchange across different models and variability within models in subpolar regions can be linked to changes in salinity stratification. We might expect this to be true for our global warming cases as well. Increased atmospheric CO_2 concentration causes an acceleration of the hydrological cycle, with greater freshwater inputs to high latitudes. This results in surface freshening while deep waters remain relatively unchanged, inhibiting convection and overturning. Increasing stratification can thus be part of a positive feedback cycle whereby fresh waters are less efficiently removed from convective regions (Gnanadesikan, Scott, et al., 2017; Stommel, 1961).

The strong linkage between stratification and vertical exchange is most clearly seen by looking at the evolution of salinity, oxygen, and age under global warming in the NW Pacific (120–180°W, 50–65°N). Figure 12 shows scatter plots where each point is an annually averaged value from our global warming simulations with different colors representing different simulations. Stratification and age at depth increase over time in all of the simulations, and oxygen decreases. In the NW Pacific, the salinity stratification is a good predictor of oxygen (Figure 12a) and age (Figure 12b) at 300 m both within and across the global warming runs (surprisingly, changes in temperature stratification in this region actually move toward being destabilizing

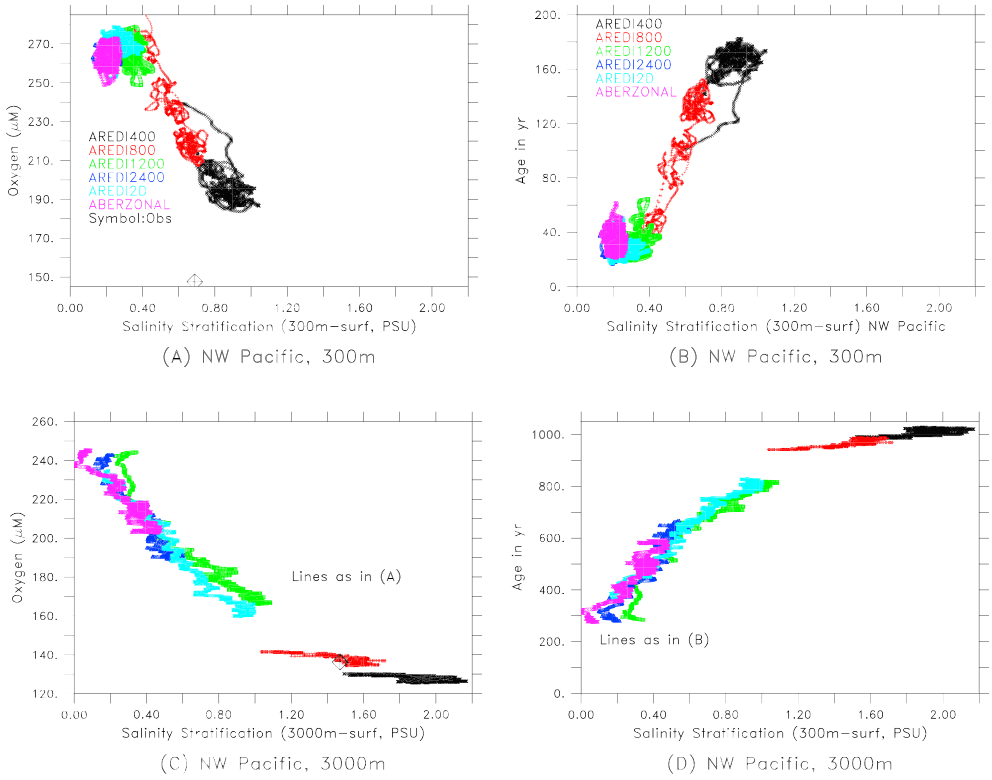

Figure 12. Scatter plot of the evolution of oxygen and age versus salinity stratification relative to the surface (salinity at depth minus salinity at the surface) under global warming. Each color represents a different mixing coefficient and each point is a single year. In those simulations where there is a significant change the movement of the system is downward and to the right for oxygen (higher stratification equals lower oxygen) and upward and to the right for age (higher stratification=higher age). (a) Oxygen at 300 m versus salinity at 300 m minus sea surface salinity. (b) Age at 300 m versus salinity at 300 m minus sea surface salinity. (c) Oxygen at 3,000 m versus salinity at 3,000 m minus sea surface salinity. (d) Age at 3,000 m versus salinity at 3,000 m minus sea surface salinity

under global warming). The fact that the point clouds overlap suggests a common mechanism for this region.

At 300 m (Figure 12a), all of these simulations start off having too much oxygen relative to modern observations, including AREDI400 which has relatively realistic levels of stratification. It turns out that AREDI400 has overturning in this region, which appears to be a little too strong and too deep (Gnanadesikan et al., 2015a, 2017). This bias (which is also found in other ESMs) may represent a source of error in simulating modern changes in oxygen, but may also result in producing overly strong deoxygenation under global warming. The biggest change in stratification and thus decline in oxygen is seen in the AREDI800 model (red points), which starts off with a stronger overturning that shuts off more or less completely. The high-mixing models, by contrast are able to maintain low stratification at 300 m and therefore see little change in oxygen at this depth (blue, green, pink, and aqua point clouds in Figure 12a).

At 3,000 m, there is a general decrease in oxygen concentration under global warming, but the largest drops are seen in the high-mixing cases (green, blue, aqua, and pink point clouds in Figure 12c). This is because at 3,000 m the low-mixing cases start off stratified and are essentially unventilated throughout (as seen from the stratification-age relationship in Figure 12d). Increasing stratification thus has little impact on oxygen concentrations at depth (red and black point clouds in Figure 12c). However, in the high-mixing cases, there is an increase in salinity stratification over time, which results in large drops in oxygen concentration at this depth (green and blue point clouds in Figure 12c, and changes in overturning in Figure 10). In this region and depth, the increase in temperature stratification does play a role in stabilizing the water column, but it is an order of magnitude less important than salinity. In contrast to the results at 300 m, the observed oxygen and stratification (symbol, Figure 12c) are closest to the initial state of the AREDI400 run (overlapping

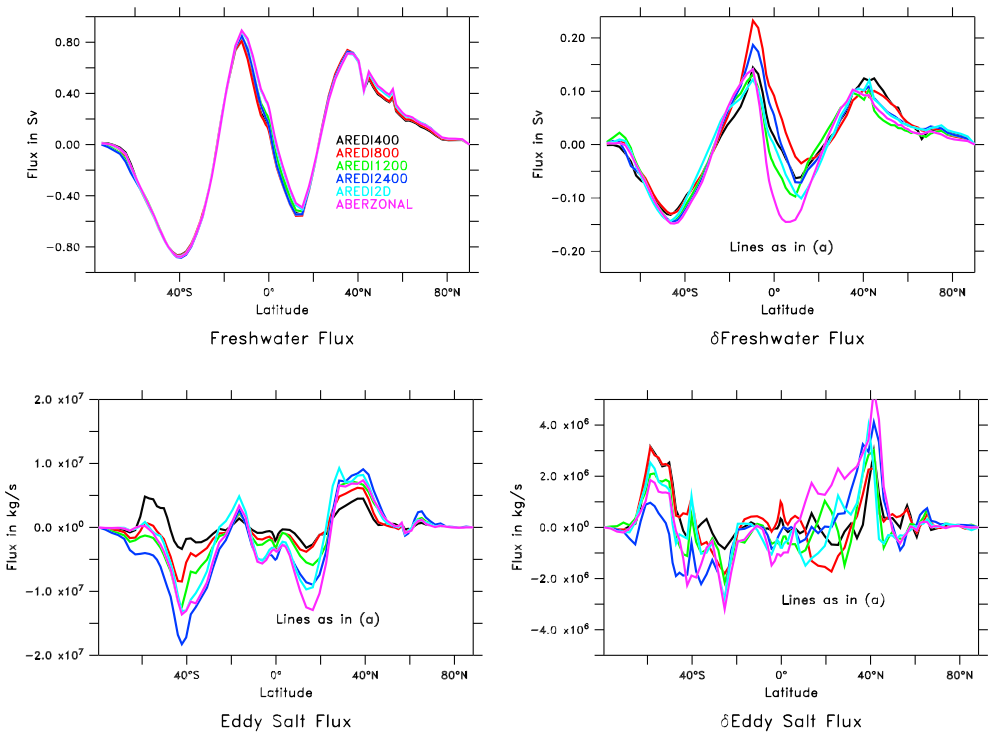

Figure 13. Time mean northward freshwater and eddy salt flux for CM2Mc model suite. The top row shows northward fluxes of fresh water (computed as the negative of the summed volume transport from top to bottom) and the bottom row shows northward salt fluxes associated with parameterized eddies (saved out separately and integrated from top to bottom). Left column shows control conditions. Right column shows the change under global warming. Note that a downward slope to the right of the freshwater flux implies freshening and lightening (making it harder to form deep water), while a downward slope to the right of salt flux implies salinification and densification (implicitly making it easier to form deep water).

the global warming case for the AREDI800 run), and the relationship between the two is generally consistent with an inverse relationship between stratification and oxygen.

The dependence of age and oxygen on stratification in Figure 12 are almost perfect mirror images. This suggests that their changes are both consequences of a locally driven decrease in ventilation. If changes in production were extremely important we would expect to see different shapes in the two point clouds. A similar correspondence is seen in the South Pacific sector of the Southern Ocean at 300 m (Figures S5a and S5b), implying that a similar decrease in local ventilation is at work here. However, in the Weddell Sea the picture is quite different (Figures S5c and S5d) with no clear relationship between local stratification and either age or oxygen, although the two fields are closely related to each other. What appears to occur here is that all models see a shutoff in deep convection in this region, resulting in a long-term adjustment of both age and oxygen to deep ocean, which is not complete at the end of the 140-year simulation. Within a single ESM, Yamamoto et al. (2015) found similar long time scales of change, with a recovery of convection in the Weddell Sea and the associated increase in deep oxygen occurring 500 years after CO_2 was doubled.

5.4.2. Salt and Freshwater Fluxes

In both the Pacific sector of the Southern Ocean and the Northwest Pacific, there are notable differences in how salinity stratification changes across the different models. These differences could be driven by the surface freshwater flux (the high-mixing models are warmer and so might be expected to transport more freshwater poleward) or by parameterized salt flux (the high-mixing models are more effective at supplying salt to high latitudes). As shown in Figure 13a, the meridional freshwater fluxes in the control models are relatively similar across the model suite while the parameterized eddy salt fluxes (Figure 13c) are quite different. As previously argued by Pradal and Gnanadesikan (2014) for the four constant A_{REDI} simulations, it is the higher mixing supplying more salt to high northern and southern latitudes that drives destabilization of these regions and increased convection. It is worth noting that even though the ABER2D and

ABERZONAL models have peak diffusivities much larger than AREDI2400, the associated salt fluxes (not previously reported) are bracketed by the AREDI1200 and AREDI2400 simulations.

Under global warming, the water fluxes show a pattern of increased export from the subtropics and increased convergence in the equatorial and subpolar regions. In northern latitudes, the largest signal is seen in the low-mixing runs (AREDI400 and AREDI800, black and red lines, respectively, in Figure 13b), but the changes are relatively similar across models particularly in high latitudes.

The same cannot be said for the changes in salt flux (Figure 13d). In the Southern Ocean, the poleward eddy salt flux *decreases* under global warming—representing a positive feedback on the salinity stratification. The decrease is anticorrelated with the mixing coefficient, but is of the same sign for all the simulations. As can be seen in Figure 1, the A_{REDI} coefficient is low in the Southern Ocean in the spatially variable mixing runs. The common decrease in salt flux may explain why all the models show a reduction of deep Southern Ocean convection. In the northern subpolar oceans, the eddy salt flux increases under global warming with the largest increases seen in the higher mixing cases. In the northern subpolar gyre, the stronger negative feedback implied by eddy salt flux changes helps explain why the changes in salinity stratification and thus vertical exchange are weaker in the higher mixing simulations.

6. Conclusions

We have shown that the value of the lateral diffusive mixing coefficient A_{REDI} can have a significant impact on the pattern of ocean deoxygenation and changes in the amount of hypoxic and suboxic waters. Cross-model differences in global mean deoxygenation are largely determined by the differences in biological drawdown which, consistent with previous work dominates at depth (Bopp et al., 2002, 2013; Cocco et al., 2013; Cabré et al., 2015; Keller et al., 2016). Rather than being driven by differences in export (and thus oxygen utilization rate) the differences across models are determined by how long the utilization of oxygen is allowed to accumulate. This in turn is controlled by deep convection in high latitudes, which is very sensitive to the value of A_{REDI}. Interestingly, the fact that biological drawdown is increasing implies that the preformed nutrient content of the ocean as a whole must decrease. While the general findings of this study are consistent with current understanding (Shepherd et al., 2017), our quantification of the impact of lateral mixing represents a new result.

Some of the lessons of our sensitivity study can be applied to the CMIP5 models. Repeating the analysis in Figure 11 for these models (Figure S6), we find that they also show tongues of oxygen decrease emanating from high latitudes and oxygen increases at middepths in the tropics. Similar to our model suite, the CMIP5 models show a significant variation in the depths to which these tongues of decreasing oxygen penetrate, the magnitude of the peak decrease and the extent to which they project onto regions that are close to being hypoxic. This helps to explain why two of the CMIP models show expansion of hypoxia outside of the tropics. In HadGEM a shutoff in overturning in the North Pacific pushes intermediate waters across the hypoxic threshold while in IPSL the slowdown of oxygen supply from the south intersects the threshold for hypoxia in the deep Pacific. Our results suggest that these cross-model differences are strongly affected by differences in deep convection. Further work is needed, however, to understand the physical balances that lead to such differences.

The pattern of tropical oxygen increase and decrease in hypoxic volume is less consistent across the CMIP5 models than it is in our model suite. This may be because models handle feedbacks between oxygen and nutrient cycling differently (particularly denitrification and nitrogen fixation, as discussed by Tyrell, 1999). Although the variation in A_{REDI} across the CMIP5 models has the potential to produce differences of similar magnitude to those seen in Figures 1 and S6, it is unlikely to be the sole driver.

As has been previously noted, the observed increase in hypoxic volumes in recent decades (Schmidtko et al., 2017) is not consistently found under global warming in the models that most reliably reproduce the oxygen profile and distribution (Oschlies et al., 2018). This could imply that the observed changes are due to natural variability connected with the Pacific Decadal Oscillation (Czeschel et al., 2012; Duteil et al., 2018; Ito & Deutsch, 2013). Alternatively, our results suggest that models which have too vigorous and stable deep convection in the North Pacific (whether because they have A_{REDI} coefficients that are too large or for some other reason) will also fail to produce the observed increase in hypoxia.

Our results with the ABER2D model suggest that implementing a more realistic spatial distribution of A_{REDI} is possible without significantly changing the simulation of oxygen. Although it would have been convenient if the zonal variation of this coefficient (represented by ABERZONAL) completely captured the impacts of a two-dimensional mixing coefficient, this does not appear to be the case. Even more work is needed to constrain the actual three-dimensional distribution of lateral mixing and to understand its changes over time. Changes in the mixing of oxygen over time have been invoked to drive changes in regions such as the tropical Atlantic (Brandt et al., 2010). Because we do not allow A_{REDI} to vary in time or in the vertical, our results should be seen at setting bounds on what a dynamic theory of mixing might be able to accomplish. Our results also suggest that mixing coefficients in some regions, particularly convective regions and the edges of OMZs, may be more important than other regions (such as the centers of the subtropical gyres). Dynamical theories for linking mixing coefficients to stratification have been proposed for idealized scenarios such as zonally uniform channels with a flat bottom, but have not been implemented in realistic climate models with realistic bathymetry. Our results emphasize how important such work is for accurate projection of oceanic biogeochemical cycling.

Acknowledgments
This work was supported by the National Oceanographic and Atmospheric Administration under grant NA16OAR4310174 and the National Science Foundation Frontiers in Earth Systems Dynamics Program under grant EAR-1135382 and by the JHU Institute for Data-Intensive Engineering and Sciences. CMIP5 model output and the observed oxygen data sets are publicly available. Output from our model suite is available at the JHU Dataverse site (https://doi.org/10.7281/T1/IWOVKD).

References

Abernathey, R. P., & Marshall, J. (2013). Global surface eddy diffusivities derived from satellite altimetry. *Journal of Geophysical Research: Oceans*, *118*, 901–916. https://doi.org/10.1002/jgrc.20066

Bentsen, M., Bethke, I., Debernard, J. B., Iversen, T., Kirkevåg, A., Seland, Ø., et al. (2013). The Norwegian Earth System Model, NorESM1-M—Part 1: Description and basic evaluation of the physical climate. *Geoscientific Model Development*, *6*(3), 687–720. https://doi.org/10.5194/gmd-6-687-2013

Bianchi, D., Dunne, J. P., Sarmiento, J. L., & Galbraith, E. D. (2012). Data-based estimates of suboxia, denitrification, and N_2O production in the ocean and their sensitivities to dissolved O_2. *Global Biogeochemical Cycles*, *26*, GB2009. https://doi.org/10.1029/2011GB004209

Bopp, L., le Quéré, C., Heimann, M., & Manning, A. C. (2002). Climate-induced oceanic oxygen fluxes: Implifcation for the contemporary carbon budget. *Global Biogeochemical Cycles*, *16*(2), 1022. https://doi.org/10.1029/2001GB001445

Bopp, L., Resplandy, L., Orr, J. C., Doney, S. C., Dunne, J. P., Gehlen, M., et al. (2013). Multiple stressors of ocean ecosystems in the 21st century: projections with CMIP5 models. *Biogeosciences*, *10*(10), 6225–6245. https://doi.org/10.5194/bg-10-6225-2013

Brandt, P., Hormann, V., Körtzinger, A., Visbeck, M., Krahmann, G., Stramma, L., et al. (2010). Changes in the ventilation of the oxygen minimum zones of the tropical North Atlantic. *Journal of Physical Oceanography*, *40*(8), 1784–1801. https://doi.org/10.1175/2010JPO4301.1

Cabré, A., Marinov, I., Bernardello, R., & Bianchi, D. (2015). Oxygen minimum zones in the tropical Pacific across CMIP5 models: Mean state differences and climate change trends. *Biogeosciences*, *12*(18), 5429–5454. https://doi.org/10.5194/bg-12-5429-2015

Cocco, V., Joos, F., Steinacher, M., Frölicher, T. L., Bopp, L., Dunne, J., et al. (2013). Oxygen and indicators of stress for marine life in multi-model global warming projections. *Biogeosciences*, *10*(3), 1849–1868. https://doi.org/10.5194/bg-10-1849-2013

Czeschel, R., Stramma, L., & Johnson, G. C. (2012). Oxygen decreases and variability in the eastern equatorial Pacific. *Journal of Geophysical Research*, *117*, C11019. https://doi.org/10.1029/2012JC008043

Diaz, R. J., & Rosenberg, R. (2008). Spreading dead zones and consequences for marine ecosystems. *Science*, *321*(5891), 926–929. https://doi.org/10.1126/science.1156401

Dunne, J. P., Armstrong, R. A., Gnanadesikan, A., & Sarmiento, J. L. (2005). Empirical and mechanistic models for the partial export ratio. *Global Biogeochemical Cycles*, *19*, GB4026. https://doi.org/10.1029/2004GB002390

Dunne, J. P., John, J. G., Adcroft, A. J., Griffies, S. M., Hallberg, R. W., Shevliakova, E., et al. (2012). GFDL's ESM 2 Global Coupled Climate–Carbon Earth System Models. Part I: Physical formulation and baseline simulation characteristics. *Journal of Climate*, *25*(19), 6646–6665. https://doi.org/10.1175/jcli-d-11-00560.1

Dunne, J. P., John, J. G., Shevliakova, E., Stouffer, R. J., Krasting, J. P., Malyshev, S. L., et al. (2013). GFDL's ESM 2 global coupled climate–carbon earth system models. Part II: Carbon system formulation and baseline simulation characteristics. *Journal of Climate*, *26*(7), 2247–2267. https://doi.org/10.1175/JCLI-D-12-00150.1

Dunne, J. P., Sarmiento, J. L., & Gnanadesikan, A. (2007). A synthesis of global particle export from the surface ocean and cycling through the ocean interior and on the seafloor. *Global Biogeochemical Cycles*, *21*, GB4006. https://doi.org/10.1029/2006GB002907

Duteil, O., Oschlies, A., & Böning, W. (2018). Pacific Decadal Oscillation and recent oxygen decline in the eastern tropical Pacific Ocean. *Biogeosciences Discussions*, 1–30. https://doi.org/10.5194/bg-2018-16

England, M. H. (1995). The age of water and ventilation timescales in a global ocean model. *Journal of Physical Oceanography*, *25*(11), 2756–2777. https://doi.org/10.1175/1520-0485(1995)025<2756:TAOWAV>2.0.CO;2

Fogli, P. G., Manzini, E., Vichi, M., Alessandri, A., Patara, L., Gualdi, S., et al. (2009). INGV-CMCC carbon (ICC): A carbon cycle Earth system model. CMCC Research Paper, 61. https://doi.org/10.2139/ssrn.1517282

Freing, A., Wallace, D. W. R., & Bange, H. W. (2012). Global oceanic production of nitrous oxide. *Philosophical Transactions of the Royal Society B: Biological Sciences*, *367*, 1245–1255. https://doi.org/10.1098/rstb.2011.0360

Frölicher, T. L., Joos, F., Plattner, G.-K., Steinacher, M., & Doney, S. C. (2009). Natural variability and anthropogenic trends in oceanic oxygen in a couple carbon cycle-climate model ensemble. *Global Biogeochemical Cycles*, *23*, GB1003. https://doi.org/10.1029/2008GB003316

Galbraith, E. D., Gnanadesikan, A., Dunne, J. P., & Hiscock, M. R. (2010). Regional impacts of iron-light colimitation in a biogeochemical model. *Biogeosciences*, *7*(3), 1043–1064. https://doi.org/10.5194/bg-7-1043-2010

Galbraith, E. D., Kwon, E. Y., Gnanadesikan, A., Rodgers, K. B., Griffies, S. M., Bianchi, D., et al. (2011). Climate variability and radiocarbon in the CM2Mc Earth system model. *Journal of Climate*, *24*(16), 4230–4254. https://doi.org/10.1175/2011JCLI3919.1

Gent, P. R. (2011). The Gent-McWilliams parameterization: 20/20 hindsight. *Ocean Modelling*, *39*(1-2), 2–9. https://doi.org/10.1016/j.ocemod.2010.08.002

Gent, P. R., & McWilliams, J. C. (1990). Isopycnal mixing in ocean circulation models. *Journal of Physical Oceanography*, *20*(1), 150–155. https://doi.org/10.1175/1520-0485(1990)020<0150:IMIOCM>2.0.CO;2

Gent, P. R., Willebrand, J., McDougall, T. J., & McWilliams, J. C. (1995). Parameterizing eddy-induced tracer transports in ocean circulation models. *Journal of Physical Oceanography*, *25*(4), 463–474. https://doi.org/10.1175/1520-0485(1995)025<0463:PEITTI>2.0.CO;2

GFDL Global Atmospheric Model Development Team (2004). The new GFDL global atmosphere and land model AM2/LM2: Evaluation with prescribed SST simulations. *Journal of Climate*, *17*(24), 4641–4673. https://doi.org/10.1175/JCLI-3223.1

Gnanadesikan, A., Bianchi, D., & Pradal, M.-A. (2013). Critical role for mesoscale eddy diffusion in supplying oxygen to hypoxic ocean waters. *Geophysical Research Letters*, *40*, 5194–5198. https://doi.org/10.1002/grl.50998

Gnanadesikan, A., Dunne, J. P., & John, J. (2012). Understanding why the volume of suboxic waters does not increase over centuries of global warming in and Earth system model. *Biogeosciences*, *9*(3), 1159–1172. https://doi.org/10.5194/bg-9-1159-2012

Gnanadesikan, A., Pradal, M.-A., & Abernathey, R. (2015a). Isopycnal mixing by mesoscale eddies significantly impacts oceanic anthropogenic carbon uptake. *Geophysical Research Letters*, *42*, 4249–4255. https://doi.org/10.1002/2015gl064100

Gnanadesikan, A., Pradal, M.-A., & Abernathey, R. P. (2015b). Exploring the isopycnal mixing and helium-heat paradoxes in a suite of Earth system models. *Ocean Science*, *11*(4), 591–605. https://doi.org/10.5194/os-11-591-2015

Gnanadesikan, A., Russell, A., Pradal, M.-A., & Abernathey, R. (2017). Impact of lateral mixing in the ocean on El Nino in a suite of fully coupled climate models. *Journal of Advances in Modeling Earth Systems*, *9*, 2493–2513. https://doi.org/10.1002/2017MS000917

Gnanadesikan, A., Russell, J. L., & Zeng, F. (2007). How does ocean ventilation change under global warming? *Ocean Science*, *3*(1), 43–53. https://doi.org/10.5194/os-3-43-2007

Gnanadesikan, A., Scott, A. A., Pradal, M. -A., Seviour, W. J. M., & Waugh, D. W. (2017). Regional responses to black carbon aerosols: The importance of Air-Sea interaction. *Journal of Geophysical Research: Atmospheres*, *122*, 12,982–12,999. https://doi.org/10.1002/2017JD027589

Griffies, S. M., Biastoch, A., Böning, C., Bryan, F., Danabasoglu, G., Chassignet, E. P., et al. (2009). Coordinated Ocean-ice Reference Experiments (COREs). *Ocean Modelling*, *26*(1-2), 1–46. https://doi.org/10.1016/j.ocemod.2008.08.007

Gruber, N., & Sarmiento, J. L. (1997). Global patterns of marine nitrogen fixation and denitrification. *Global Biogeochemical Cycles*, *11*(2), 235–266. https://doi.org/10.1029/97GB00077

Hsia, C. C. W., Schmitz, A., Lambertz, M., Perry, S. F., & Maina, J. N. (2013). Evolution of air breathing: oxygen homeostasis and the transitions from waste to land and sky. *Comprehensive Physiology*, *3*(2), 849–915. https://doi.org/10.1002/cphy.c120003

Ilyina, T., Six, K. D., Segsschneider, J., Maier-Reimer, E., Li, H., & Núñez-Riboni, I. (2013). Global ocean biogeochemistry model HAMOCC: Model architecture and performance as component of the MPI-Earth system model in different CMIP5 experimental realizations. *Journal of Advances in Modeling Earth Systems*, *5*, 287–315. https://doi.org/10.1029/2012MS000178

Ito, T., & Deutsch, C. (2013). Variability of the oxygen minimum zone in the tropical North Pacific during the late twentieth century. *Global Biogeochemical Cycles*, *27*, 1119–1128. https://doi.org/10.1002/2013GB004567

Ito, T., & Follows, M. (2005). Preformed phosphate, soft-tissue pump and atmospheric CO_2. *Journal of Marine Research*, *63*(4), 813–839. https://doi.org/10.1357/0022240054663231

Keeling, R. E., Körtzinger, A., & Gruber, N. (2010). Ocean deoxygenation in a warming world. *Annual Review of Marine Science*, *2*(1), 199–229. https://doi.org/10.1146/annurev.marine.010908.163855

Keller, D. P., Kriest, I., Koeve, W., & Oschlies, A. (2016). Southern Ocean biological impacts on global ocean oxygen. *Geophysical Research Letters*, *43*, 6469–6477. https://doi.org/10.1002/2016GL069630

Klocker, A., & Abernathey, R. (2014). Global patterns of mesoscale eddy properties and diffusivities. *Journal of Physical Oceanography*, *44*(3), 1030–1046. https://doi.org/10.1175/jpo-d-13-0159.1

Kwon, E. Y., Deutsch, C., Xie, S.-P., Schmidtko, S., & Cho, Y.-K. (2016). The North Pacific oxygen uptake rates over the past half century. *Journal of Climate*, *29*(1), 61–76. https://doi.org/10.1175/JCLI-D-14-00157.1

Marinov, I., Gnanadesikan, A., Sarmiento, J. L., Toggweiler, J. R., Follows, M., & Mignone, B. K. (2008). Impact of ocean circulation on biological carbon storage in ocean and atmosphere pCO_2. *Global Biogeochemical Cycles*, *22*, GB3007. https://doi.org/10.1029/2007GB002958

Matear, R. J., & Hirst, A. C. (2003). Long-term changes in dissolved oxygen concentrations in the ocean caused by protracted global warming. *Global Biogeochemical Cycles*, *17*(4), 1125. https://doi.org/10.1029/2002GB001997

Mislan, K. A. S., Deutsch, C. A., Brill, R. W., Dunne, J. P., & Sarmiento, J. L. (2017). Projections of climate-driven changes in tuna vertical habitat based on species-specific differences in blood oxygen affinity. *Global Change Biology*, *23*, 4019–4028. https://doi.org/10.1111/gcb.13799

Nevison, C., Butler, J. H., & Elkins, W. (2003). Global distribution of N_2O and the N_2O-AOU yield in the subsurface ocean. *Global Biogeochemical Cycles*, *17*(4), 1119. https://doi.org/10.1029/2003GB002068

Oschlies, A., Brandt, P., Stramma, L., & Schmidtko, S. (2018). Drivers and mechanisms of ocean deoxygenation. *Nature Geoscience*, *11*(7), 467–473. https://doi.org/10.1038/s41561-018-0152-2

Palmer, J. R., & Totterdell, I. J. (2001). Production and export in a global ocean ecosystem model. *Deep Sea Research Part I: Oceanographic Research Papers*, *48*(5), 1169–1198. https://doi.org/10.1016/S0967-0637(00)00080-7

Peña, M. A., Katsev, S., Oguz, T., & Gilbert, D. (2010). Modeling dissolved oxygen dynamics and hypoxia. *Biogeosciences*, *7*(3), 933–957. https://doi.org/10.5194/bg-7-933-2010

Pradal, M.-A., & Gnanadesikan, A. (2014). How does the Redi parameter for mesoscale mixing impact global climate in an Earth system model? *Journal of Advances in Modeling Earth Systems*, *6*, 586–601. https://doi.org/10.1002/2013MS000273

Praetorius, S. K., Mix, A. C., Walczak, M. H., Wolhowe, M. D., Addison, J. A., & Prahl, F. G. (2015). North Pacific deglacial hypoxic event linked to abrupt ocean warming. *Nature*, *527*(7578), 362–366. https://doi.org/10.1038/nature15753

Redi, M. H. (1982). Ocean isopycnal mixing by coordinate rotation. *Journal of Physical Oceanography*, *12*, 1154–1158.

Schmidtko, S., Stramma, L., & Visbeck, M. (2017). Decline in global oceanic oxygen content during the past five decades. *Nature*, *542*(7641), 335–339. https://doi.org/10.1038/nature21399

Shepherd, G., Brewer, P. G., Oschlies, A., & Watson, A. J. (2017). Ocean ventilation and deoxygenation in a warming world: Introduction and overview. *Philosophical Transactions of the Royal Society A*, *375*(2102), 20170240. https://doi.org/10.1098/rsta.2017.0240

Stommel, H. (1961). Thermohaline convection with two stable regimes of flow. *13*(2), 224–229. https://doi.org/10.1111/j.2153-3490.1961.tb00079.x

Stramma, L., Johnson, G. C., Firing, E., & Schmidtko, S. (2010). Eastern Pacific oxygen minimum zones: Supply paths and multidecadal changes. *Journal of Geophysical Research*, *115*, C09011. https://doi.org/10.1029/2009JC005976

Stramma, L., Prince, E. D., Schmidtko, S., Luo, J., Hoolihan, J. P., Visbeck, M., et al. (2012). Expansion of oxygen minimum zones may reduce available habitat for tropical pelagic fishes. *Nature Climate Change*, *2*(1), 33–37. https://doi.org/10.1038/nclimate1304

Thiele, G., & Sarmiento, J. L. (1990). Tracer dating and ocean ventilation. *Journal of Geophysical Research*, *95*(C6), 9377–9391. https://doi.org/10.1029/JC095iC06p09377

Tyrell, T. (1999). The relative influences of nitrogen and phosphorus on oceanic primary production. *Nature*, *400*(6744), 525–531. https://doi.org/10.1038/22941

Vaquer-Sunyer, R., & Duarte, C. (2008). Thresholds of hypoxia for marine biodiversity. *Proceedings of the National Academy of Sciences of the United States of America*, *105*(40), 15,452–15,457. https://doi.org/10.1073/pnas.0803833105

Wen, N., Frankignoul, C., & Gastineau, G. (2016). Active AMOC-NAO coupling in the IPSL-CM5A-MR climate model. *Climate Dynamics*, *47*(7-8), 2105–2119. https://doi.org/10.1007/s00382-015-2953-y

Yamamoto, A., Abe-Ouchi, A., Shigemitsu, M., Oka, A., Takahashi, K., Ohgaito, R., & Yamanaka, Y. (2015). Global deep ocean oxygenation by enhanced ventilation in the ocean under long-term global warming. *Global Biogeochemical Cycles*, *29*, 1801–1815. https://doi.org/10.1002/2015GB005181

Ying, B., & Yangchun, L. (2016). Simulations of dissolved oxygen concentration in CMIP5 Earth system models. *Acta Oceanologica Sinica*, *35*(12), 28–37. https://doi.org/10.1007/s13131-016-0959-x